A comparative study of platinum nanodeposits on HOPG (0001), MnO(100) and MnOx/MnO(100) surfaces by STM and AFM after heat treatment in UHV, O2 , CO and H2

Tsybukh, R.

CHAPTER 5

Manganese oxide surfaces starting from a MnO(100) single-crystal surface

This chapter describes atomic force microscopy imaging of the topography of a MnO(100) single-crystal surface after annealing under reducing/inert (ultra-high vacuum, Ar) and oxidizing (O_2) conditions. Several MnO(100) samples were also annealed at an atmospheric pressure of Ar (at 1000 and 1100°C) and O_2 (700 °C) in a rapid thermal annealing furnace. Thermal annealing treatments of a MnO(100) surface resulted in the development of several distinct surface structures. The influence of the annealing conditions on the behavior of the surface structures was studied. Taking into account the literature data and the Mn_xO_y phase diagram the formation, morphology and the phase composition of the observed surface structures are discussed.

5.1 Introduction and literature review: manganese oxides and their surfaces

This section presents basic data on manganese oxides and some of their surfaces.

Due to the variable valence of manganese cations the chemistry of its compounds is very rich. This holds true for manganese oxides as well. There are several stable manganese oxides that also occur as minerals. MnO occurs in nature as a green-colored mineral manganosite and has a so-called rocksalt structure which can be considered as the insertion of two *fcc* lattices, which are build up of Mn^{2+} and O^{2-} ions [Fig 5.1 (A)]. Other common manganese oxides having manganese in higher oxidation state are: Mn_3O_4, Mn_2O_3 and MnO_2. The first one known as the mineral hausmannite at ambient temperature has a distorted spinel structure and can be represented by the formula $Mn^{2+}[Mn_2^{3+}]O_4^{2-}$ [1]. Two polymorphs of this oxide exist, named α and β. Also, there are two polymorphs of Mn_2O_3 known as minerals α-kurnakite and β-kurnakite/bixbyite, respectively [2]. The most stable and common among manganese dioxides in nature - the mineral pyrolusite (β-MnO_2) has a simple tetragonal rutile (TiO_2) structure [1, 3]. This oxide has a variety of polymorphs [1-3]. Hence, it can be anticipated that the surfaces of manganese oxides having exposed metal atoms are particularly prone to change their oxidation state at proper conditions, consequently surface structures evolving due to these processes may be quite complex. To begin tackling this issue it is useful to know the routes of the manganese oxides transformation under different conditions. This subject has been discussed in many papers [4-17] and

except for some metastable phases, the main transformation routes and their thermodynamics are quite well understood and documented [4, 8, 11]. In Fig. 5.1 the unit cell dimensions and the lattice parameters are listed while in Fig. 5.2 a summary of the literature data on the transformations of stable Mn oxides is presented.

The identification and research of various Mn oxides are hampered by severe difficulties: many specimens are found as brittle, poorly crystallized materials and are often mixtures of several oxides [18, 19]. Because of these reasons many questions still remain on the structure of some naturally occurring Mn oxide mineral specimens, especially on some polymorphic and metastable whose stability regions are not clearly established [17-19]. At the same time their synthetic counterparts are mostly very difficult to grow as single-crystals. Some Mn oxide phases are also difficult to analyze using conventional analytical techniques and equipment. Due to these complications the growth dynamics and the surface structure of manganese oxide specimens are very little explored.

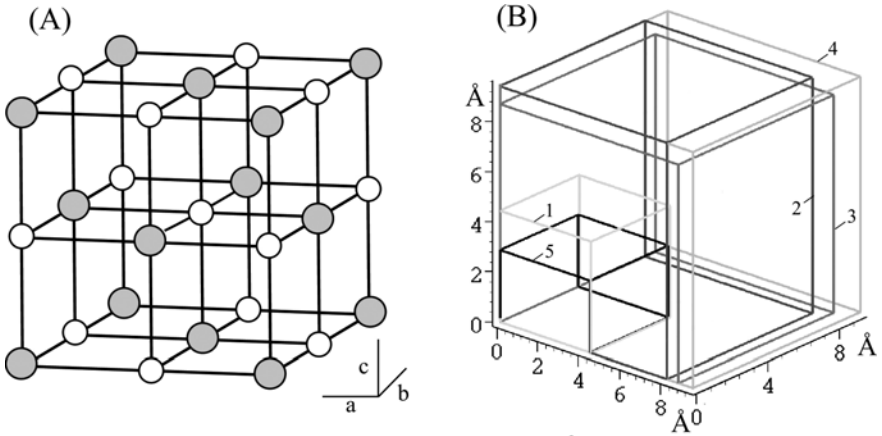

Lattice parameters (Å)

1.	MnO	Cubic	a=b=c=4.44
2.	$\alpha - Mn_3O_4$	Tetragonal	a=b=8.14; c=9.42
3.	$\beta - Mn_3O_4$	Cubic	a=b=c=8.7
4.	$\beta - Mn_2O_3$	Cubic	a=b=c=9.41
5.	$\beta - MnO_2$	Tetragonal	a=b=4.4; c=2.87

Figure 5.1: ***(A)*** *Rocksalt structure of MnO. The gray spheres represent* O^{2-} *and the white spheres represent* Mn^{2+} ***(B)*** *Schematic illustration of the unit cell dimensions of stable manganese oxides [1-3].*

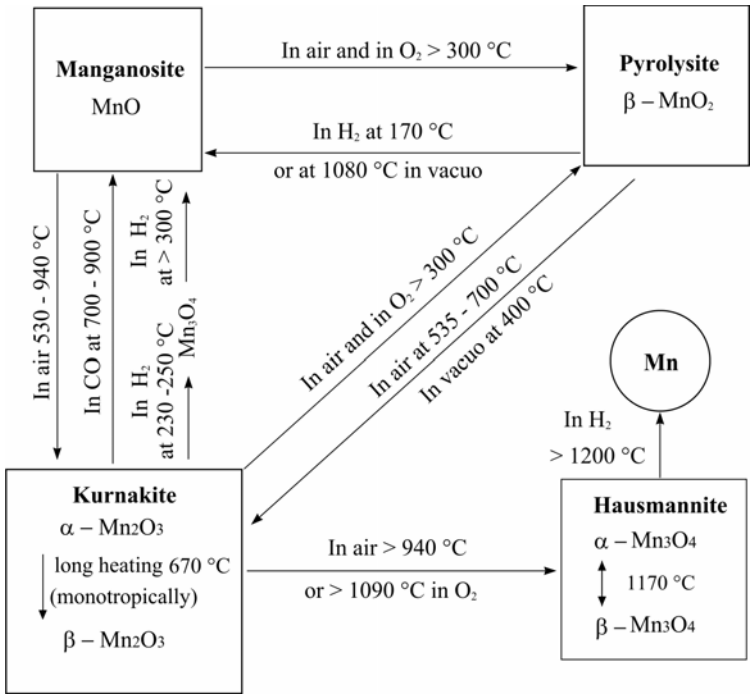

Figure 5.2: *Schematic illustration of the transformations of manganese oxides under different conditions according to literature data [4-6, 17-19, 20-23].*

In early studies some mineral Mn oxide specimens have been analyzed [24-27] and morphological analysis of some powdered manganese oxides obtained from different precursors has been accomplished [28-30]. According to [28] a Mn_3O_4 phase, prepared using different precursors had a very broad particle size distribution ranging from several to 100 nm, some cubic particles were observed, but many particles did not exhibit a well-defined shape. Mn_3O_4 particles prepared from MnO_2 had a tetragonally distorted cubic shape with a size of about 25 to 40 nm. Recently, several studies on the preparation of MnO, Mn_2O_3 and Mn_3O_4 phases of nanosize dimensions were performed [31-36]. Generally, depending on the precursor a variety of nanostructures were registered ranging from polyhedrons and globular structures to nanorod structures. Ahmad *et al.* [31] via manganese oxalate precursor under specific reaction conditions synthesized cubic nanoparticles of MnO (28 nm) and α-Mn_2O_3 (50 nm).

In the present research as a starting point for the investigations of the surface structure of manganese oxides, the thermodynamically stable MnO(100) surface [37] was chosen. MnO is an antiferromagnetic wide band gap material that results from the localized band structure characteristic for the late cubic 3d transition metal (TM) monoxides [38, 39]. There is rather good agreement

between its energy gap of 3.6-3.8 eV determined experimentally [40] and theoretically by self-consistent Hartree energy band calculation [41]: 4.8 eV (in good agreement with optical absorption measurements), *ab initio,* self-interaction–corrected, local-spin-density calculations [42]: 3.6-3.8 eV, as well as the most recent DFT calculations [43]: 4.02 eV. For the other manganese oxides: Mn_3O_4, Mn_2O_3, MnO_2 there is a shortage of data regarding their band gaps. Recently, by DFT calculations [44] an attempt was made to determine the band gap of these oxides and a quite broad span of its value has been found: 0.0-4.1 eV and 0.0-2.4 eV for α-Mn_2O_3 and Mn_3O_4, respectively. For β-MnO_2 the authors calculated two values of the electronic gap: 0 and 1.5 eV.

The electronic structure of TM oxides with a rocksalt structure (NiO, FeO, CoO, MnO) have been studied intensively, both theoretically [38-53] and experimentally [45, 54-65]. However, only recently it was possible to image some of their single-crystal surfaces with atomic resolution using STM at elevated temperatures [66-70] and AFM [71-75]. In recent years one observes steadily increasing interest concerning the preparation of the thin films of MnO as well as higher Mn-oxides. Up to present time they were grown on several metal and oxide substrates [76-91]. Some of these systems were analyzed using scanning probe microscopy [76-78, 83, 85, 86, 91]. However, the investigations of the MnO single-crystal surfaces are scarce. The insulating nature of MnO greatly complicates its analysis by conventional surface science probes due to static charging of the samples. In addition, it is very sensitive to any kind of treatments that is commonly used for the preparation of surfaces. Of relevance to the present research is the work carried out by Langell *et al.* [45] using MnO(100) single-crystals grown by the arc image method. Thus, it is practical to highlight its main results. According to the authors X-ray photoelectron (XP) spectra of the as-prepared MnO(100) sample indicated a reasonably clean and stoichiometric surface while high resolution electron energy loss spectroscopy (HREEL) spectra pointed to a poor quality. Annealing of the sample in oxygen [$p(O_2)=5\times10^{-7}$ Torr] at 625 K gradually increased the oxygen content in the near surface region as registered by XPS. However, the change was slow and only after 30 min a slight decrease in the O 1s/Mn 2p ratio was detected. This was attributed to desorption of surface carbonates and to the surface reduction through reactions with carbon-containing adsorbates. Longer annealing at the same conditions gradually increased the O/Mn ratio and after 2.5 h the ratio has increased by 1.5. The 2p satellite features characteristic of the MnO also gradually disappeared and the 2p binding energies have shifted to higher values. The authors attributed these results to the formation of the Mn_2O_3 phase. The HREEL spectrum, however, exhibited ill-defined features with energies of the peaks similar to those observed in the as-introduced sample. The oxide continued to show an inferior (1×1) LEED pattern of the MnO(100) surface. No further changes were observed upon heating in UHV

for periods of 1 h until the temperature was increased to 775 K. At this point by HREELS indications of the formation of an oxide with well-defined order but with a symmetry lower than that expected for cubic MnO(100) have been found. On the basis of these results, XPS analysis of binding energies and the O/Mn intensity ratio of 1.3, the formation of the Mn_3O_4 phase was suggested. Continued annealing of this sample to higher temperature (1000 K) for 10 min resulted in the XP and HREEL spectra characteristic of the MnO(100) surface. However, the satellites below each of the two Mn 2p peaks characteristic of the Mn monoxide were less distinct as expected for stoichiometric MnO. The O/Mn intensity ratio was only about 80 % of that expected for MnO(100). The authors stated that the Mn_2O_3, Mn_3O_4 and MnO phases are in roughly epitaxial relation to the MnO(100) substrate and that it is difficult to isolate pure epitaxial layers of a certain oxide due to the ready formation and intermixture of the oxide specimens.

Because of the above mentioned complications in the present study the characterization of the MnO(100) surface was performed by AFM. This technique is a powerful tool for the investigation of the surface structure of various materials [92-94].

In this chapter the temperature-dependent evolution of the topography of a MnO(100) surface after thermal annealing treatments under reducing and oxidizing conditions is presented. Annealing in UHV conditions was performed in a vacuum < 10^{-9} mbar.

5.2 Results

This section presents the results of AFM imaging of a MnO(100) single-crystal after annealing in UHV, in the presence of oxygen at low as well as atmospheric pressure, and in an atmosphere of argon. Attempts to image the surface of an as-received MnO(100) single-crystal and the samples after any of the performed annealing experiments by STM at ambient temperature were not successful. The performed experiments revealed the formation of several types of surface structures on the MnO(100) surface after the temperature treatments.

5.2.1 Thermal annealing treatment of the MnO(100) surface in UHV

(A) Annealing in the UHV set-up

The topography image of an as-received MnO(100) single-crystal is shown in Fig. 5.3 (A). The surface shows polishing streaks some nanometers in depth. Apart from the artifacts caused by polishing, some of 2D and/or 3D particles of unknown

origin were also detected. Probably they are due to the nucleation of some new phase, e.g., manganese hydroxide(s)/oxyhydroxide(s). This effect is known for polished MgO single crystals exposed to the ambient water vapor [95]. Zooming in, however, revealed a rather rough surface, as shown in Fig. 5.3 (B). The root mean square roughness, R_{rms}, i.e. standard deviation of the height value, averaged for several images was 0.6 nm on a 1×1 μm^2 scale.

LEED analysis revealed somewhat diffuse spots of the (1×1) structure of the MnO(100) surface at a potential starting from 150 eV with progressively increasing brightness of the spots to 270 eV. The LEED pattern of the MnO(100) surface is shown as an inset in Fig. 5.3 (A).

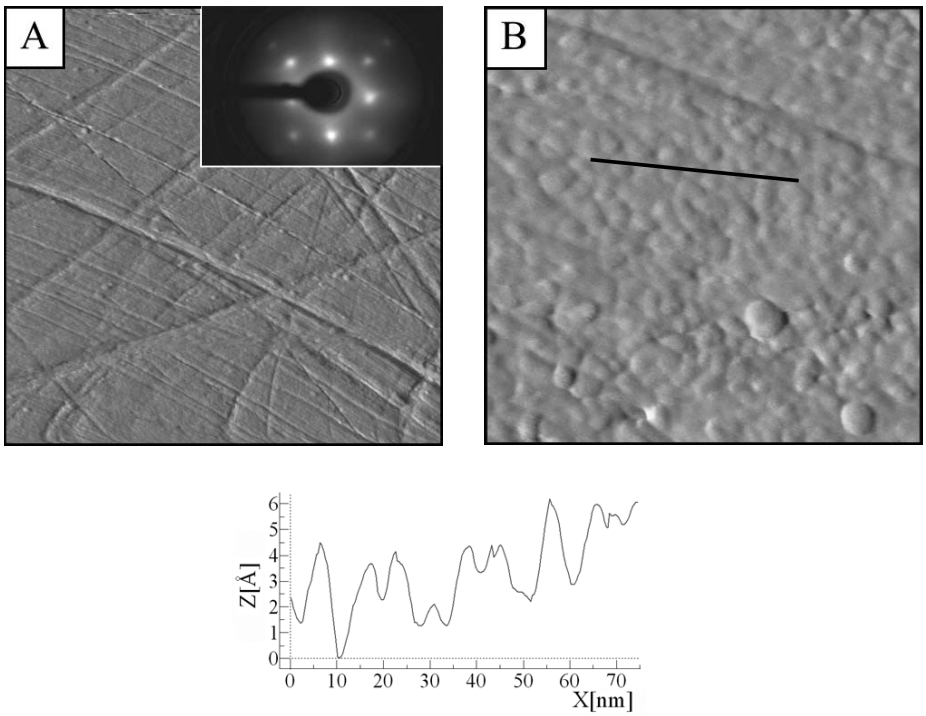

Figure 5.3: *AFM images (contact mode) of an as-received MnO(100) crystal.* ***(A)*** *(1500 × 1500 nm²). The inset shows a (1 × 1) LEED pattern obtained for this sample at 270 eV.* ***(B)*** *(150 × 150 nm²). The black line indicates the position of the height profile shown below the images.*

Since there is no "recipe" for the preparation of a clean and smooth MnO(100) surface, several treatments have been tried. In the following the sets of performed experiments are presented.

An as-received MnO(100) single-crystal was subjected to various annealing cycles of about 30 minutes in UHV in the temperature range of 400-560 °C (total annealing time 2.5 h). It should be noted that after each temperature treatment AFM imaging registered some changes of the surface topography but not dramatic in comparison with the initial surface structure. The temperature of annealing was then increased to 580 °C. Imaging of the sample after annealing for 30 minutes at this temperature revealed that the surface morphology radically was changed into elongated straight structures, as shown in Fig. 5.4. Further in the text it will be termed as the rippled-like structure (RLS). It is seen from the AFM images that the structure is quite homogeneously distributed all over the surface. Its height, as can be seen from the cross-line section in Fig. 5.4 (C) is about 1-2 nm. An interesting fact is that the RLSs in many sites of the surface are situated along two perpendicular directions to each other. Apparently, the structure follows the cubic symmetry of the underlying MnO(100) substrate and is aligned along the principal axes (001) and (010). However, because the contact mode of the AFM being not able to provide true atomic resolution of the substrate the exact orientation of the structures is unknown. In addition to the RLS, square depressions (pits) could

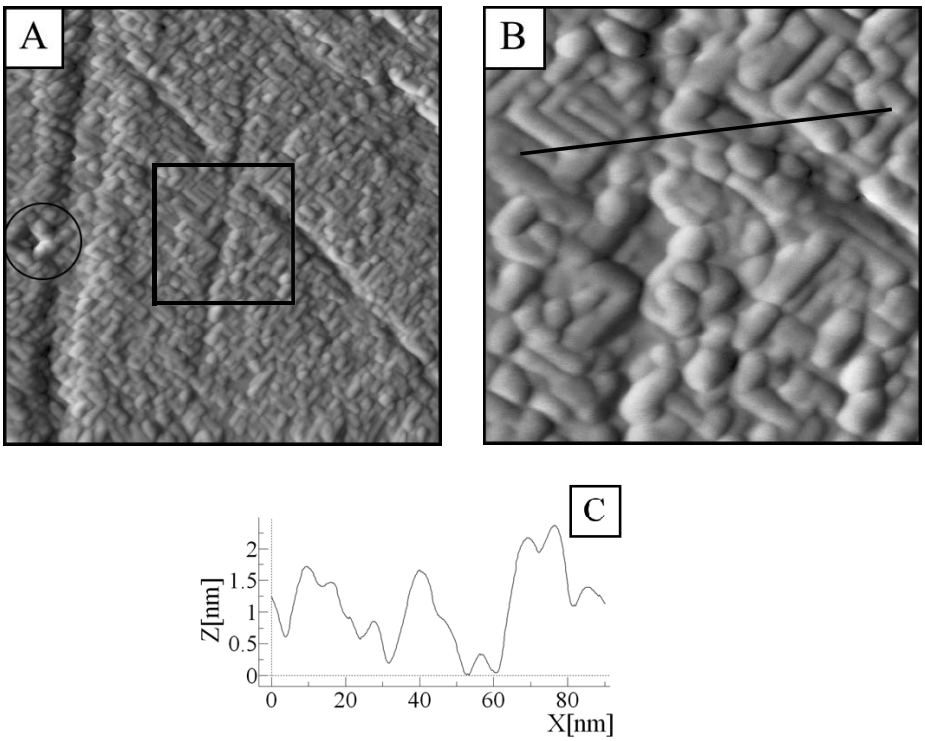

Figure 5.4: *AFM image of an as-received MnO(100) surface after 30 min annealing in UHV at 580 °C. Image size:* ***(A)*** *(300 × 300 nm²).* ***(B)*** *(100 × 100 nm²).* ***(C)*** *A cross-line section taken along the black line in* ***(B)****.*

occasionally be observed on the surface. Upon further annealing at higher temperature (650 °C) for 80 min the RLS appears to flatten out, preserving their elongated shape and perpendicular position to each other (Fig. 5.5). However, at the same time, some locations of the surface became less densely covered with the RLSs. The observed number of the pits is now larger as seen on the large scale image [Fig. 5.5 (A), encircled]. They range from 4 to 11 nm in depth with external sides 20-50 nm, with the majority having sides of 40 nm. The maximum dimension of the pits is *ca.* 50×50 nm. Their sidewalls are inclined by about 45° with respect to the pits' bottom plane as deduced from the line profiles of the AFM images [see, e.g., Fig. 5.5 (D)]. Interestingly that not all sidewalls within the pits exhibit are "monolithic" but frequently are composed of several smaller steps, as seen in Fig. 5.5 (C, D). However their inclination and, consequently crystallographic orientation is difficult to determine from the line profiles. We suggest that the formation of the pits may be connected with the presence of some kind of defects in the near-surface region, e.g., dislocations, nanovoids that have been formed during the growth process of the crystal. Upon annealing the material diffused out from these areas that led to the formation of the pits. Some of the pits are arranged in rows, which probably correspond to dislocation networks.

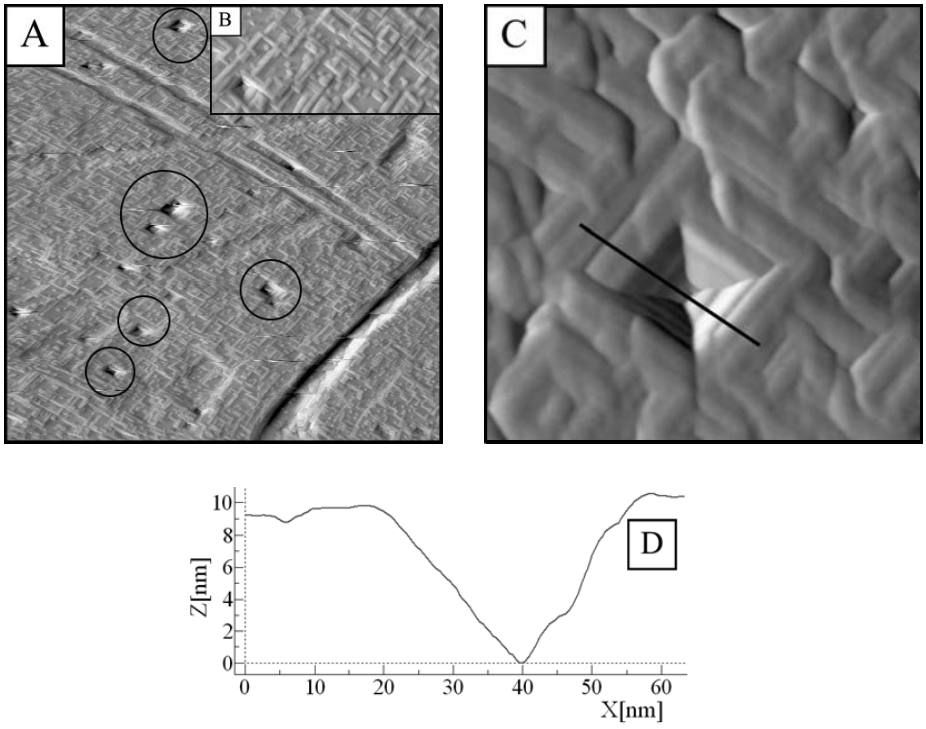

Figure 5.5: *AFM image of the MnO(100) sample after further annealing in UHV at 650°C for 80 min (total time of the annealing 170 min). Image size:* ***(A)*** *1.5 × 1.5 μm². (B) The inset (300 × 145 nm²).* ***(C)*** *150 × 150 nm².* ***(D)*** *A cross-line section taken along the black line.*

The rectangular shape of the pits presumably results from the surface energies of the sidewalls – apparently they are higher than the surface energy of the (100) face of MnO. This also may be the factor that limits the pits' size. Subsequent annealing of the sample for 2 h in UHV at 645 °C caused the RLS to disappear completely and the surface topography became as depicted in Fig. 5.6.

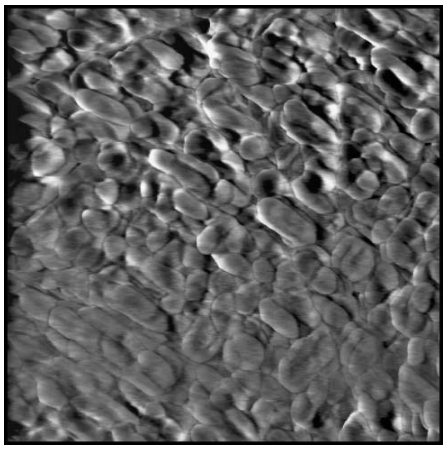

Figure 5.6: *AFM image (800 × 800 nm²) of the MnO(100) sample after annealing in UHV at 645 °C for 2 h.*

Quite unexpectedly further annealing of this sample at an increased temperature of 700 °C for 1.5 h resulted in the reappearance of a very distinct RLS [Fig. 5.7 (A)] which persisted even after an additional annealing cycle at 700 °C for 2.5 h [Fig. 5.7 (B)]. At some surface locations the elongated structure exhibited a very regular pattern. The width of some of the elongated structures was exactly 10 and 20 nm. Yet another annealing cycle of the crystal at the same temperature for1 h caused the structure to flatten out (Fig. 5.8). Intrigued by such behavior of the surface it was interesting to explore if annealing of the same sample in oxygen could influence the surface morphology. Thus, the sample was subjected to annealing in oxygen [$p(O_2)=3\times10^{-6}$ mbar] at 700 °C for 4 h. This caused further disintegration of the remnants of the RLS to even smaller elongated structures (Fig. 5.9).

On the basis of this set of experiments it is concluded that the RLS appears after annealing of the MnO(100) sample for at least 30 min at 580 °C. It is stable to some extent but longer annealing at increasing temperature (above 645 °C) causes its deterioration. When the crystal was annealed in UHV at higher temperature (700 °C) and for 1.5 and 2.5 h the RLS appeared again. But shorter annealing (1 h) at 700 °C makes the structure flatter and wider. Subsequent annealing under a low pressure of oxygen at the same temperature but for a longer time (4 h) had a further deteriorative effect on the structure and made it to split apart to even

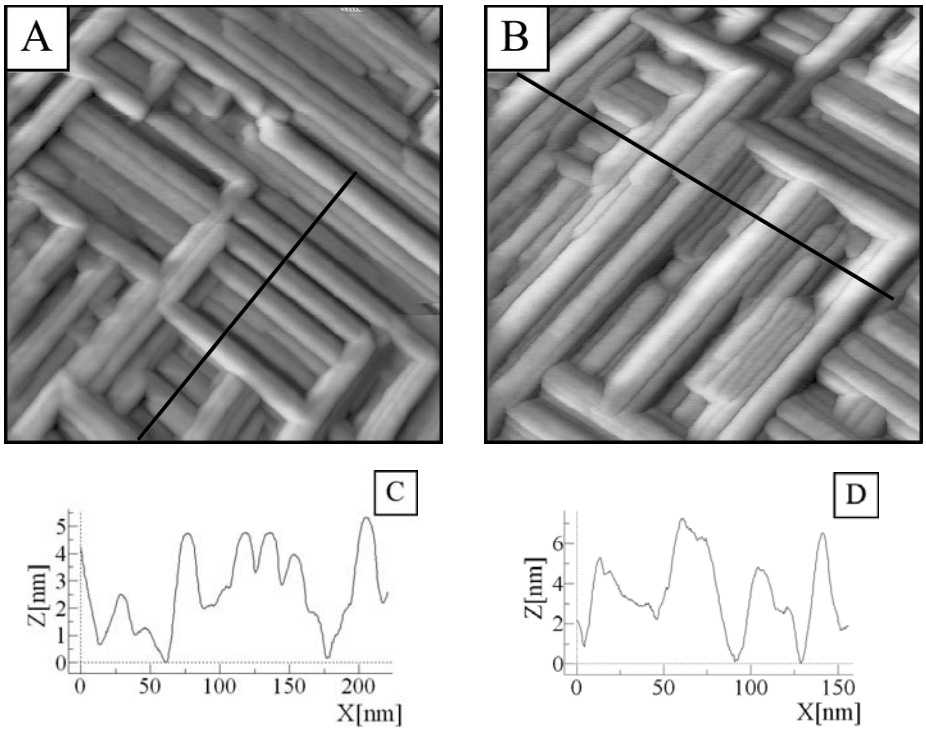

Figure 5.7: *AFM images of the MnO(100) sample after annealing in UHV at 700 °C for 1.5 h* ***(A)*** *(280 × 280 nm²) and* ***(B)*** *further annealing at 700° C for 2.5 h (150 × 150 nm²).* ***(C)*** *and* ***(D)*** *cross-line sections taken along the black line in* ***(A)*** *and* ***(B)****, respectively.*

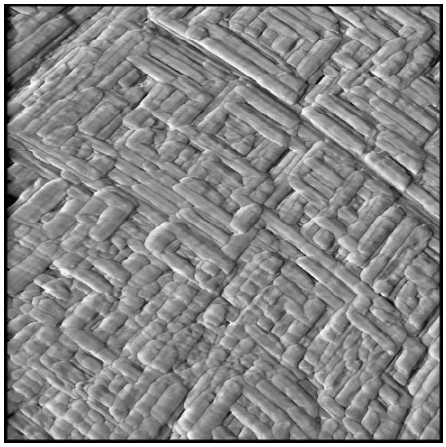

Figure 5.8: *AFM image (800 × 800 nm²) of the MnO(100) sample after annealing in UHV at 700° C for 1 h.*

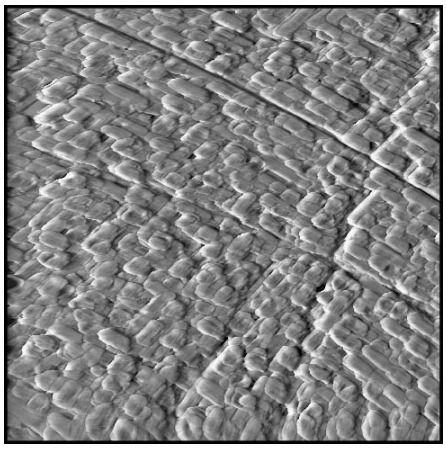

Figure 5.9: *AFM image (1000 × 1000 nm²) of the MnO(100) sample after annealing in oxygen p(O_2)= 3 × 10^{-6} mbar at 700 °C for 4 h.*

smaller and flatter elongated islands. Based on these results we suppose that changes of the surface topography of the MnO samples: appearance of the RLS, its dissemblance and reappearance might result from oxygen loss in the near surface area during annealing as well as oxygen diffusion from the bulk to the surface. This model is substantiated by the fact that Mn-oxides can easily loose or incorporate lattice oxygen in response to a heat treatment. For example, as was found in [96], partial loss of lattice oxygen of MnO_2 probably occurs already at 550°C. The metastable Mn_5O_8 phase loses oxygen above 550 °C to form α-Mn_2O_3 [97, 98]. In addition, in the most recent papers [99, 100] it has been reported that the surface phase-transformation from α-Mn_2O_3 to Mn_3O_4-like specimens occurs only at or above 450 °C in the presence of pure He or in a mixture of O_2 + CH_4. It was supposed that this transformation is due to the loss of lattice oxygen at high temperatures that leads to the surface reconstruction. Interestingly, a reversible phase-transformation also was observed with decreasing the temperature to 25 °C. Probably, similar processes also can occur in the MnO single-crystal during annealing/cooling cycles. It is interesting to note that MnO is capable to take up oxygen to $MnO_{1.13}$ without any change of lattice or development of a new phase [20]. The structural changes in the crystal may impact the processes of Mn/O diffusion. This in turn may influence the temperature of the surface structure transformations. Perhaps the heating/cooling time also influences the balance of Mn/O delivery to the surface, thus the surface structure. A preliminary model regarding the origin of the formation, morphology and phase composition of the RLS is given in the Discussion.

***(B)** Annealing an as-received MnO(100) sample at atmospheric pressure of argon in the RTAF followed by annealing in UHV*

An as-received MnO(100) sample was first annealed in the UHV setup at 650°C for 4 h and subsequently annealed at an increased temperature (750 °C) for 30 min. AFM images taken after each of the annealing cycles are shown in Fig. 5.10. As seen, this time the thermal annealing in UHV did not lead to the formation of the RLS, but instead the surface became covered with particle-like structures. The streaks due to polishing are still present on the surface. The sample was then subjected to further annealing under a constant flow of argon (1atm) in a RTAF according to the protocol: 1 min heating up to 1000 °C, annealing at this temperature for 10 min and cooling down to room temperature in about 7 min. The temperature decrease down to about 400 °C occurred in about 0.5 min. Unlike annealing in the UHV setup, where the sample heats up and cools down while mounted on a sample manipulator stick, the RTAF permits to reach the desired temperature of annealing in much shorter time. In addition, fast cooling down to

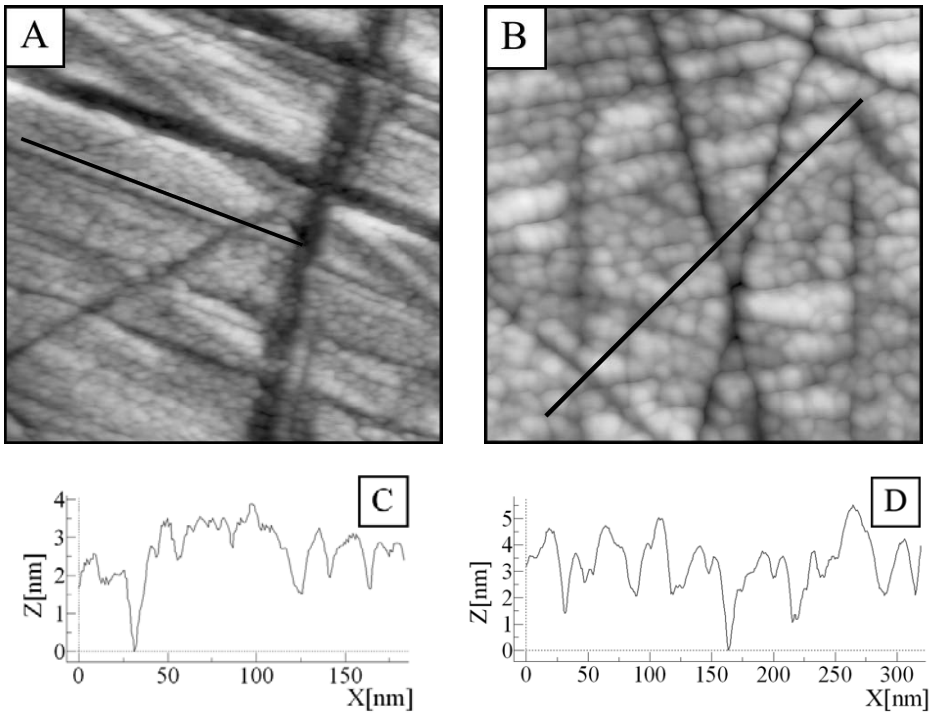

Figure 5.10: ***(A)** AFM image of the MnO(100) surface after annealing in UHV at 650 °C for 4 h. **(B)** AFM image of this sample after further annealing in UHV at 750 °C for 30 min. Size of both images 300 × 300 nm². **(C)** and **(D)** cross-line sections taken along the black line in **(A)** and **(B)**, respectively.*

ambient temperature can also be realized easily. The AFM image of the crystal after such a treatment is shown in Fig. 5.11. As can be seen, the surface exhibits rather large irregularly shaped grains with a height of about 2-4 nm. Their lateral size of the grains significantly increased in comparison with the treatment carried

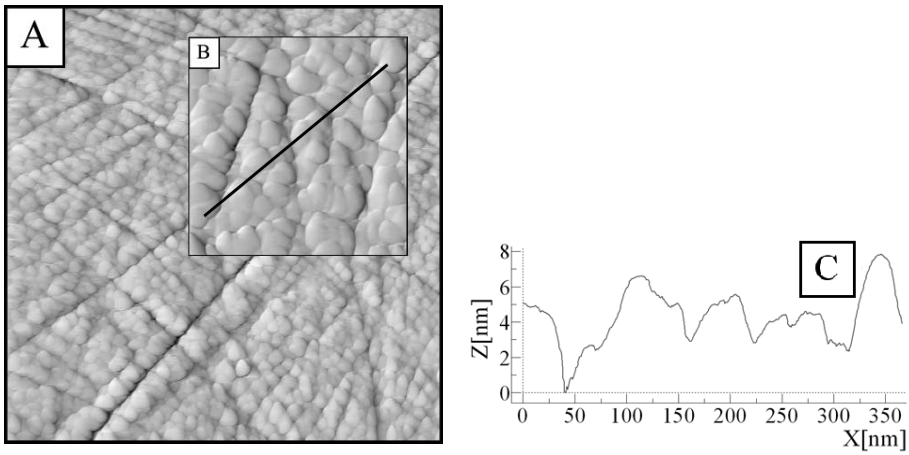

Figure 5.11: *AFM image of the MnO(100) sample after annealing in the RTAF at 1000°C for 10 min under a flow of Ar (1atm). Image size:* ***(A)*** *1000 × 1000 nm². (B) The inset (300 × 300 nm²).* ***(C)*** *A cross-line section taken along the black line.*

out in UHV at 750 °C for 30 min. The streaks due to polishing are still visible on the surface. Afterwards, the crystal was again annealed at 1000 °C in the RTAF for 10 min under a constant flow of argon according to the protocol described above. Interestingly, after such treatment the RLS of similar morphology as in the sets of experiments described in § 5.2.1 (A) appeared again, as seen in Fig. 5.12. Again in many regions of the surface the elongated structures are situated along two directions perpendicular to each other, but now the structure covers the surface less densely than in the experiments described in § 5.2.1 (A).

Based on the results of this section and those described in section 5.2.1 (A) we can conclude that heating cycles at temperatures ~ 400-650 °C prior to heating at higher temperatures is required to achieve the formation of the RLS. The structure forms on the MnO(100) surface annealed in UHV and under atmospheric pressure of Ar. Here for the formation of the RLSs we propose the same model as has been discussed in § 5.2.1 (A). More detailed investigations of the annealing procedure of the crystal may help to understand the origin of the formation of this structure.

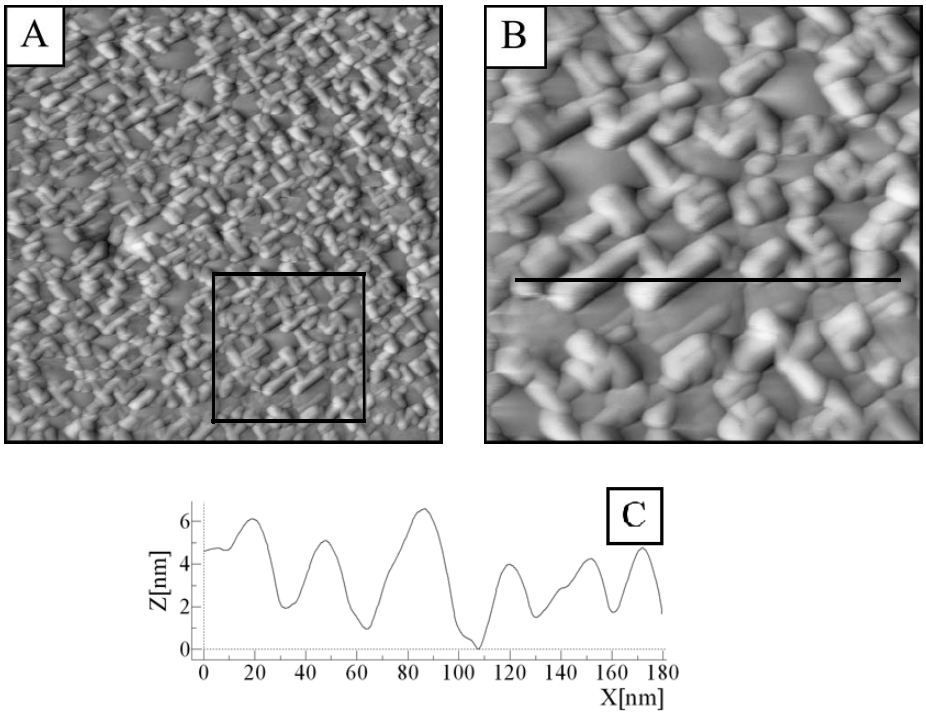

Figure 5.12: *AFM image of the MnO(100) sample after the second annealing in the RTAF at 1000 °C for 10 min under flow of Ar (1 atm). Image size:* ***(A)*** *500 × 500 nm². (B) Image (200 × 200 nm²) of the location indicated by the black square in (A).* ***(C)*** *A cross-line section taken along the black line in* ***(B)****.*

5.2.2 Annealing of the MnO(100) surface at a low pressure of oxygen

The next set of experiments was carried out with an as-received MnO(100) single-crystal under oxidizing conditions. Initially the sample was annealed in an oxygen atmosphere $p(O_2)=5\times10^{-5}$ mbar at 400 °C for 4 h. Immediately after this treatment the surface was covered with trapezoid-like pillars (TLPs), as shown in Fig. 5.13. A line-profile made approximately along the median line of the TLPs as illustrated in Fig. 5.13, revealed that their height was about 20 nm and the width was in the range of 250-300 nm. Thus, the structures, probably, grow according to the VW mode (see § 3.1). However, one also cannot exclude the possibility of the formation of these surface structures according to the Stranski–Krastanov growth mode, especially if we take into account their rather ordered arrangement on the surface. Small protrusions are visible on top of each pillar. Apparently, the protrusions represent some part of the material that was not able to incorporate into the TLPs during the growth process due to the cessation of annealing and cooling the crystal to ambient temperature. However, it cannot be excluded that

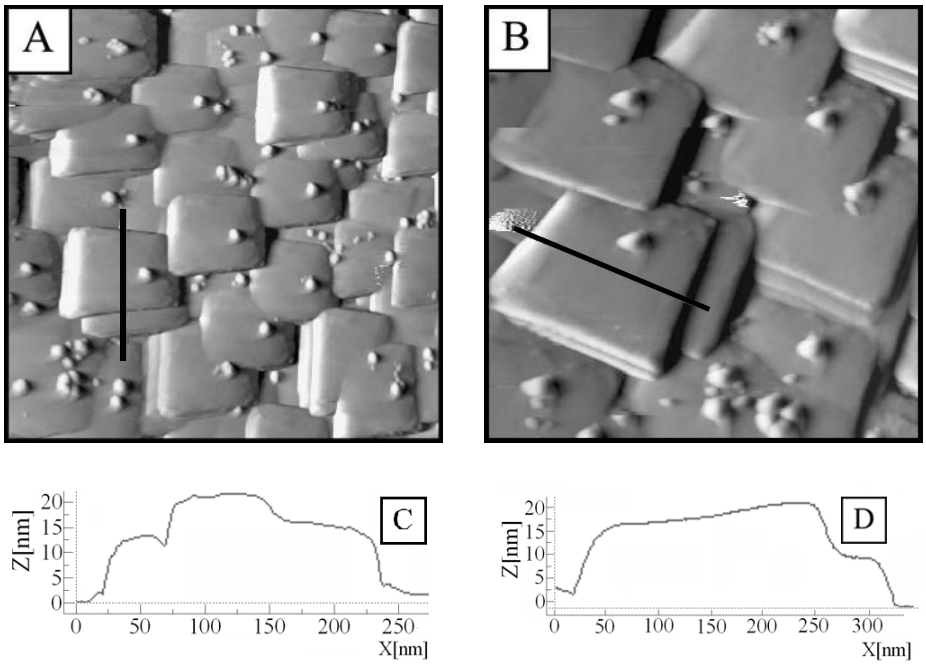

Figure 5.13: *AFM images of a MnO(100) surface after annealing in oxygen $p(O_2)=5\times10^{-5}$ mbar at 400 °C for 4 h. Image size:* ***(A)*** *(1000 × 1000 nm²).* ***(B)*** *(600 × 600 nm²). In* ***(B)*** *the scan direction of the tip is changed as compared to* ***(A)****.* ***(C)*** *and* ***(D)*** *- cross-line sections taken along the black line in* ***(A)*** *and* ***(B)****, respectively.*

the protrusions are contaminations segregated to the surface. Interestingly, after keeping the sample for 4 days in the UHV setup, the shape and dimensions of the TLPs have almost not changed, but their surfaces became quite rough (Fig. 5.14). Apparently, the roughness appeared as a result of redistribution and/or decomposition of the "particle-like" structures under the influence of the UHV environment in which very small amounts of hydrogen and water were present. The smaller scale AFM images displayed in Fig. 5.13 (B) and 5.14 (B) were obtained after changing the scanning direction with respect to the large scale image to rule out tip effects. As can be seen, the image is not affected by the scanning direction. The origin, the models of the TLPs formation and their phase composition are discussed in the Discussion.

5.2.3 High temperature annealing of the MnO(100) surface in a rapid thermal annealing furnace under argon and oxygen

In order to obtain information on how MnO(100) surface reacts at high annealing temperatures with rapid heating and cooling rates, several experiments were performed using a rapid thermal annealing furnace. To compare these sets of

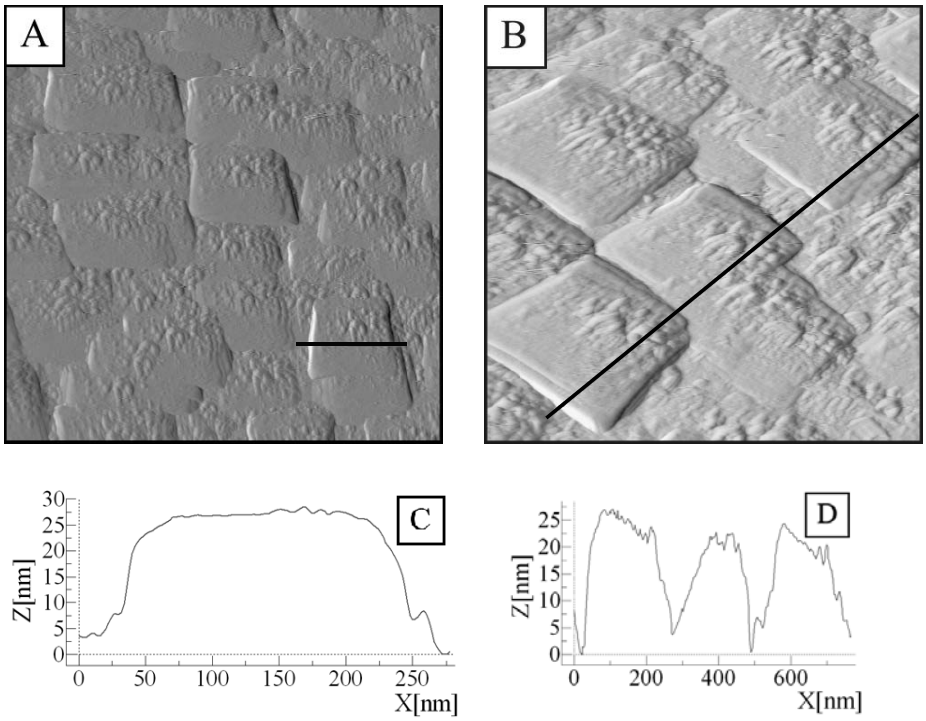

Figure 5.14: *AFM images of a MnO(100) surface after annealing in oxygen $p(O_2)=5\times10^{-5}$ mbar at 400 °C for 4 h measured after 4 days in the setup. Image size:* ***(A)*** *(1000 × 1000 nm²).* ***(B)*** *(700 × 700 nm²).* ***(C)*** *and* ***(D)*** *cross-line sections taken along the black line in* ***(A)*** *and* ***(B)****, respectively.*

experiments to those carried out in the UHV set-up, rapid thermal annealing of the MnO(100) single-crystal was carried out under a flow of argon and oxygen. At first, an as-received MnO(100) crystal was subjected to annealing under a constant flow of argon according to the protocol: 1 min heating up to 1100 °C, annealing at this temperature for 10 min and cooling down to room temperature in *ca.* 7 min. It should be noted that in this case the temperature decrease down to about 400 °C occurred in about 0.5 min. The AFM images (Fig. 5.15) after this procedure reveal that the surface is covered with rather large grains having a height of about 40 nm and a very smooth top sides. However, atomic resolution on the smooth top sides could not be obtained. At some locations of the surface hut-like regions [encircled in Fig. 5.15 (B)] with sides inclined to the probed surface at nearly 45° were imaged. Further annealing of the sample in Ar at 1100 °C for 20 and then for 40 min according to the same protocol, resulted in a slight increase of the size of the grains. Longer annealing was not carried out, but it is possible that an even more uniform surface with a small number of larger grains may be obtained at this annealing temperature. Large and almost perfectly smooth regions on the crystal surface may indicate that there is an epitaxial recrystalization of the surface.

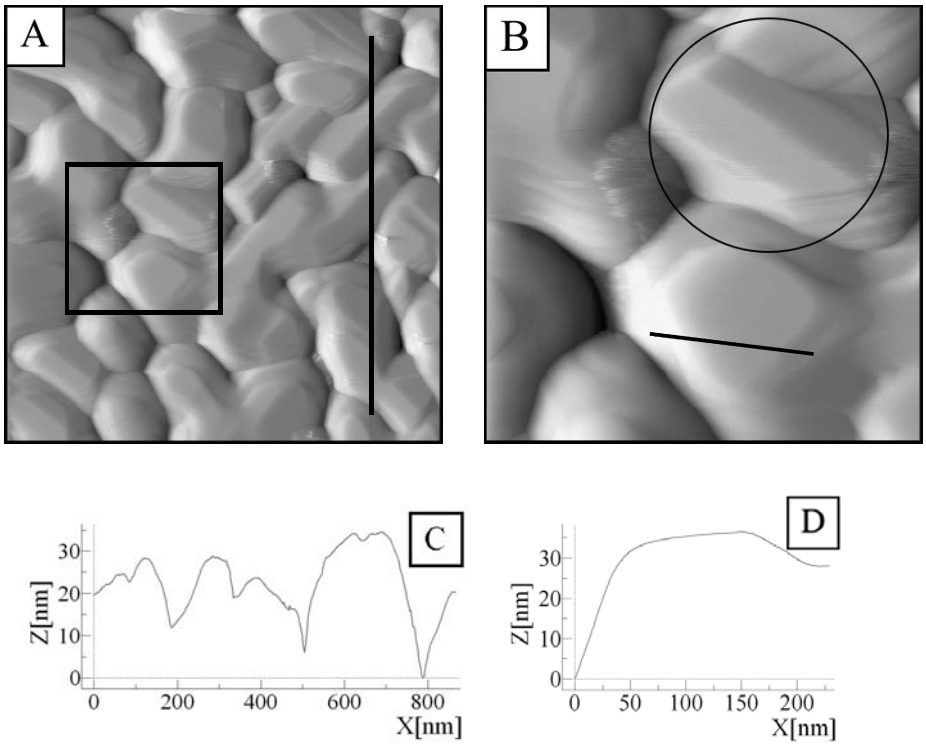

Figure 5.15: *AFM image of a MnO(100) surface after 1 min heating up to 1100 °C, annealing at this temperature for 10 min and cooling down to room temperature in about 7 min under a flow of Ar (1 atm). Image size:* ***(A)*** *945 × 945 nm². (**B**) The location of the surface (380 × 380 nm²) comprised in the square in the image (A).* ***(C)*** *and* ***(D)*** *cross-line sections taken along the black line in* ***(A)*** *and* ***(B)****, respectively.*

After the last high temperature annealing, the crystal was analyzed by XRD and the results are shown in Fig. 5.17 (C).

Another as-received MnO(100) sample was annealed at 700 °C in an atmosphere of oxygen. Initially the heating at this temperature was performed for 5 min according to the protocol described above and subsequently the sample was annealed for 20 min and then for 1 h under the same conditions. The morphology of the surface after each successive annealing cycle resembled that as depicted in Fig.5.16, i.e., a rough surface with a network of irregularly shaped grains separated by grooves which were up to 40 nm in depth. The only observed difference is that the grains on the surface become larger after each successive treatment in comparison to the first one. After the last annealing in O_2, the crystal was also analyzed by XRD [Fig. 5.17 (B)].

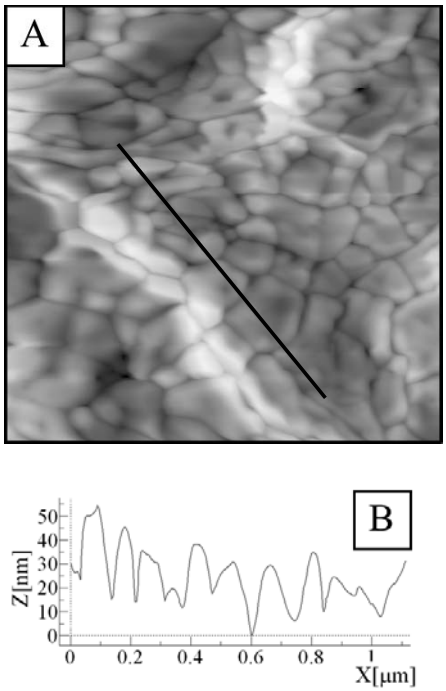

Figure 5.16: ***(A)*** *AFM image (1500 × 1500 nm²) of a MnO(100) surface subjected to annealing in O_2 (1atm) in the RTAF at 700 °C for 85 min.* ***(B)*** *A cross-line section taken along the black line.*

5.3 XRD, XPS and RBS analysis of the samples

5.3.1 XRD analysis of the samples

Obviously the morphological changes observed on the surface of the MnO(100) crystals as a result of the heat-treatments are accompanied by changes in the phase composition of the near-surface region. To address the latter issue and to answer the question how the single-crystal reacts as a whole on the particular annealing procedure X-ray diffraction analysis of some MnO(100) samples was performed.

Taking into account the mass absorption coefficients of the elements in MnO [101, 102] for the X-rays used in this study (see Chapter 2), the attenuation length or "mean free path" of the X-rays in MnO is estimated to be of *ca.* 6 μm.

In Table 5.1 and Fig. 5.17 the results of the XRD analysis are presented. An as-received MnO(100) sample exhibited two strong peaks at 2θ=40.55° and 2θ=87.74° characteristic of (200) and (400) diffraction reflections, respectively of MnO [103]. The XRD pattern also displayed rather intensive peaks at 2θ=36.50° and 2θ=44.39°, matching the (211 or 202) and (220) reflections, respectively and

minor peaks at 2θ=37.89°, 2θ=51.65° and 2θ=77.53°, matching the (004), (105) and (404) reflections, respectively of the Mn_3O_4 phase or γ-Mn_2O_3 [103].

After several cycles of annealing in a flow of O_2 at 700 °C the XRD lines characteristic of MnO have not changed their positions, but their width, as clearly seen in Fig. 5.17 (B), has decreased. It indicates an improvement of the crystal structure. This can be caused by relaxation of the strain in the crystal due to the

Table 5.1: *XRD analysis of the MnO(100) single-crystal after different temperature treatments.*

Treatment	An as-received MnO(100)	After annealing at 700 °C in O_2 for 85 min	After annealing at 1100 °C in Ar (1 atm) for 70 min
	-	32.69	31.08
	36.50	36.50	36.50
	37.89	37.94	37.96
	40.55	40.57	40.53
2 θ	44.39	44.16	44.84
	51.65	51.64	51.64
	77.53	77.56	77.55
	87.74	87.75	88.75
	98.26	97.60	97.65

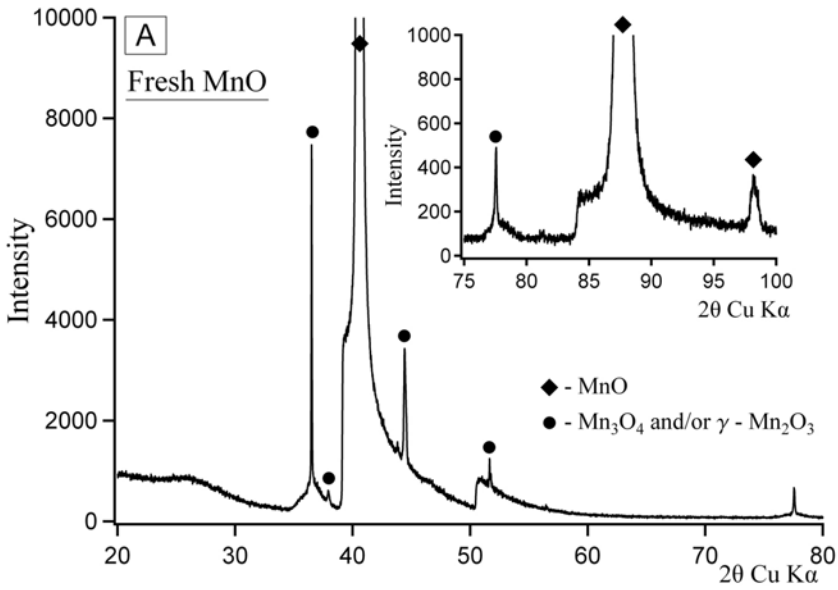

Figure 5.17: *X-ray diffraction pattern: (A) an as-received MnO(100) sample.*

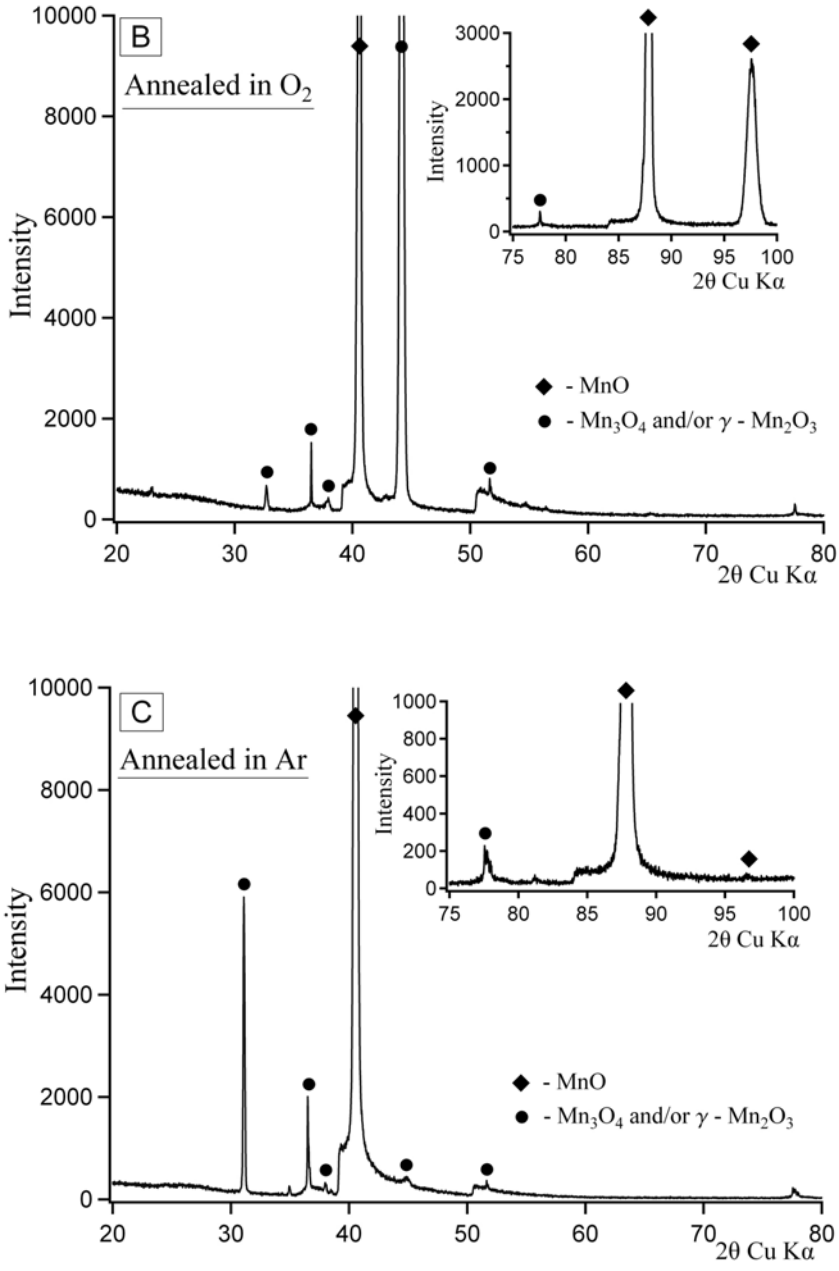

Figure 5.17: (continued) *(B) MnO(100) sample annealed several times (85 min total) in the RTAF at 700 °C under a constant flow of O_2 (1atm). (C) MnO(100) sample annealed several times (70 min total) in the RTAF at 1100 °C under a constant flow of Ar (1atm).*

healing of some defects as a result of the annealing procedures. At the same time, a peak at 2θ=44.39° is now slightly shifted to 2θ=44.16° and its intensity greatly increased. The (211 or 202) reflection of the Mn_3O_4 phase substantially decreased. In addition, a minor peak at 2θ=32.69°, coinciding with the (103) reflection of Mn_3O_4 appeared, almost unchanged the (004) and (105) reflections and weakened the (404) reflection of Mn_3O_4.

Apparently, upon annealing in O_2 the amount of the Mn_3O_4 phase in the MnO(100) sample increases and/or its crystal structure improves. Considering this result it is interesting to note that already in the earlier study by electron spin resonance spectroscopy [104] the Mn_3O_4 impurity in nonstoichiometric MnO single-crystals has been detected. It was found that the formation of Mn_3O_4 clusters in MnO occurred primarily on the surface of MnO. Moreover, it was inferred that the clusters of Mn_3O_4 in MnO were polycrystalline and almost spherical in shape. Also Lad and Henrich [63], by XRD analysis of a powder sample made from a part of a MnO single-crystal (exhibiting a high quality Laue X-ray diffraction pattern) also found the Mn_3O_4 phase in a concentration of about 7 %. An UHV-cleaved single-crystal of another TM oxide with a rocksalt structure, CoO was found to be covered by an epitaxially oriented Co_3O_4 layer [65]. Similar observations are reported in [105] for an air-exposed CoO single-crystal; the surface was Co_3O_4-terminated and this phase extended several layers beneath the surface. Also, for powdered CoO samples Co_3O_4 was found [67]. These data and our findings indicate that Mn_3O_4 can be present in the pristine MnO(100) single-crystals and also can form as a result of annealing in oxygen.

After several annealing cycles in Ar at 1100 °C, the reflection lines characteristic of MnO in the XRD pattern become much narrower in comparison with an as-received sample. A peak at 2θ=31.08° coinciding with the (200) reflection of the Mn_3O_4 phase appeared which was present neither in an as-received MnO(100) sample nor in the sample annealed in oxygen. The intensity of a peak at 2θ=36.50° was almost the same as in the annealed in the oxygen sample. The (220) reflection present in the XRD pattern of the two above described samples almost vanished and shifted to 2θ=44.84°. Also, the (004) and (105) XRD lines of Mn_3O_4 somewhat diminished.

Taking into account these results it is concluded that the crystal structure of the MnO(100) crystal improves after annealing in oxygen and Ar and possibly the amount of the Mn_3O_4 somewhat increases, and/or its structure improves. Also, it is possible that the Mn_3O_4 phase in the annealed samples is arranged differently with respect to the MnO phase than in the pristine MnO(100) sample.

5.3.2 XPS analysis of the samples

Since it is impossible to correlate the observed surface structures to a particular manganese oxide(s) phase by using AFM alone, complementary surface analytical techniques are needed. XPS is widely accessible in comparison with other surface science techniques. However, since XPS was not available in the preset setup, it was difficult to carry out a systematic analysis and therefore we attempted to examine only some of the samples.

It should be noted that the unambiguous determination of the oxidation state by XPS is only possible in the case of monophase compounds. For multiphase systems having different oxidation states with a small difference in the photoemission binding energies, such as, e.g., vanadium oxides [106], the analysis becomes much more complicated. The same kinds of difficulties arise in the XPS analysis of manganese oxides. More specific, the determination of the Mn oxidation state in Mn-oxides with a standard XPS setup is impeded for several reasons. The Mn ions are in a high spin state that causes the broadening of the Mn 2p doublet due to multiplet splitting [107, 108] and for this reason it is difficult to analyze it quantitatively. The peak maxima of the 2p core levels of Mn^{2+}, Mn^{3+}, Mn^{4+} ions are separated only by about 1 eV. This makes the separation of the contribution of each oxidation state to the XPS spectrum quite difficult, even with the application of deconvolution methods.

XPS studies of MnO, either as a single-crystal, or as a supported phase on other substrates, were carried out in [80, 109-116]. The best procedure to distinguish the Mn oxidation states seems to be the employment of a combination of the Mn 2p doublet binding energy, the Mn 2p satellite structure, the Mn 3s multiplet splitting and valence band spectra [113]. The Auger parameter method [117] employed in [113] for Mn-oxides determination is also capable to provide rather good results. However, the differences in the position of the Auger lines (LMM) of Mn in different oxidation states are not large enough and the line is rather broad that complicates the analysis. Recently, it was shown that valence-band photoemission spectroscopy can serve as an effective complementary tool to core-level studies to distinguish the various manganese oxides [118].

XP spectra of an as-received MnO(100) single-crystal are presented in Fig. 5.18 and the results of the determination of the binding energies of the elements are summarized in Table 5.2. To compensate for charging effects the spectra were referenced to the C 1s level of carbon at 284.4 eV. All the characteristic peaks of MnO(100) are well resolved and the binding energies of the Mn 3s and Mn 2p levels are in good agreement with literature data. But, instead of the two shake-up satellites generally observed 6 eV below each of the two spin-orbit-split Mn 2p peaks [118] only one weak satellite below the Mn $2p_{3/2}$ peak is present. These

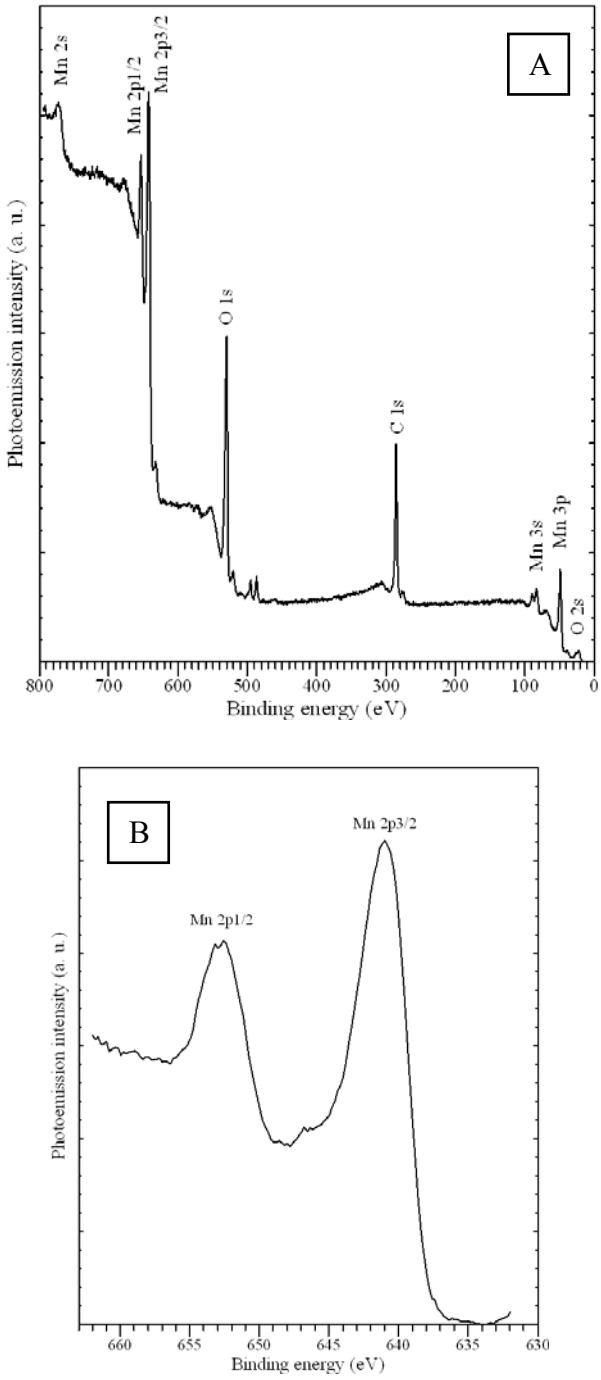

Figure 5.18: ***(A)*** *XPS of an as-received MnO(100) single crystal. High-resolution XPS of an as-received MnO(100) single crystal.* ***(B)*** *Mn2p level.*

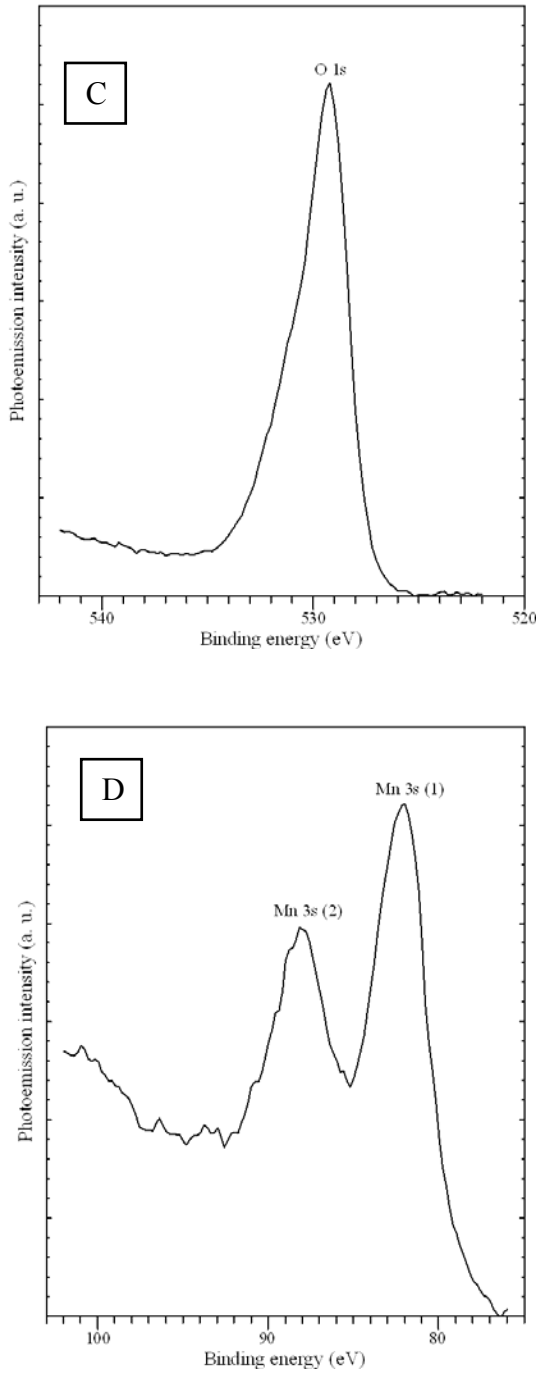

Figure 5.18: (continued) *(C) O1s level, (D) Mn3s level.*

Table 5.2: *XPS binding energies (eV) of the MnO(100) samples treated in (UHV, O_2, Ar).*

Sample	O1s	$Mn2p_{3/2}$	$Mn2p_{1/2}$	Mn3s (1)	Mn3s (2)
An as-received MnO(100)	529.2	641.0	652.8	82. 0	88.0
MnO(100) annealed in UHV at 650 °C for 4 h	530.0	640.2	653.0	#	#
MnO(100) annealed in O_2 (1atm) at 700 °C for 85 min	530.3	640.1	652.9	#	#
MnO(100) annealed in Ar (1atm) at 1100 °C for 70 min	529.8	640.2	652.0	#	#

Note: # - not measured

satellites are particularly sensitive to the stoichiometry of the oxide and disappear in higher Mn-oxides [45]. Also the disappearance of the satellites was registered by XPS of somewhat hydroxylated MnO(100) surface [116]. Hence, the XPS spectrum observed in the present study in the Mn 2p region of the pristine MnO(100) surface can stem from the two above mentioned reasons. Surface hydroxylation of a MnO(100) single-crystal due to its exposure to the atmosphere cannot be excluded. However, there were no changes in the XPS spectrum of O 1s peak [Fig. 5.18(C)] that are observed when the surface is hydroxylated [116]. Note that hydroxyl species from this surface can be removed by annealing to 200 °C [116]. For an as-received MnO(100) single-crystal we found that the splitting of the Mn 3s peak is equal to 6.0 eV and the intensity ratio of the split components is equal to 1.5, which is somewhat higher than the theoretical value of 1.4 [80]. The XP spectra of the samples annealed in Ar and O_2 were similar to the XP spectrum of an as-received MnO(100) sample. But the oxygen peak shows a little higher binding energy in all the annealed samples in comparison with an as-received sample, with the highest value observed in the sample annealed in oxygen. The Mn $2p_{3/2}$ and Mn $2p_{1/2}$ peaks are centered almost at the same value in all examined samples.

5.3.3 RBS analysis of the samples

The knowledge of the phase composition of the near-surface region of the crystal may allow its correlation with the observed surface structures. As discussed above, it is difficult to get this information by conventional XPS technique. Also, XRD in

standard diffraction geometry cannot provide such information. However, the XRD experiments described in § 5.3.1 indicate that the near-surface region (~ 6 μm) of an as-received MnO(100) crystal contains a small amount of Mn_3O_4. Another technique that can deliver similar kind of information is Rutherford backscattering spectrometry. In particular, this technique allows measuring the bulk composition and concentration profiles near the surfaces of thin homogenous films of a wide range of compounds with a depth resolution of about 10 nm. For instance, it was demonstrated that it can be successfully applied to measure the near surface composition of fresh and non-stoichiometric reduced rutile (TiO_2) single-crystal samples [119]. Therefore, it was decided to use RBS as an additional tool to determine the oxygen/manganese ratio in the near-surface region in the MnO(100) samples.

In the present study, RBS spectra of an as-received MnO(100) crystal and MnO(100) surface annealed at 700 °C for 85 min in oxygen (1 atm) were collected. Figure 5.19 and figure 5.20 show the backscattering yield from the first and the last sample, respectively along with the simulation made by RUMP program. The best fit to the RBS spectrum of an as-received MnO(100) single-crystal was obtained with the atomic ratio O/Mn=0.59/0.41 and for the sample annealed in oxygen O/Mn=0.51/0.49. The differences in normalized backscattering yield confirm that the oxidation process has induced a change of chemical composition in the MnO(100) crystal. Thus, the near surface region of an as-received MnO(100) single-crystal is oxygen enriched. Presumably, this is the result of long exposure of the crystal to the ambient atmosphere. After the sample was annealed in oxygen at 700 °C, the Mn/O ration became almost stoichiometric. The sampling depth of the He^+ ions was in the range of 1.5-2.4 μm as established from the fits to the spectra by using the RUMP simulation program. It should be noted that in RBS depths are typically expressed as an areal density of atoms and not as simple lengths. The conversion from atoms/cm^2 to angstroms, e.g., can be accomplished if the sample density is known. If this characteristic of a material is not known accurately the resultant depth scale will be in error. The variation in composition as a function of depth may cause variation in density. Therefore, we have not proceeded further in the establishing of concentration profiles of the elements in the MnO(100) samples.

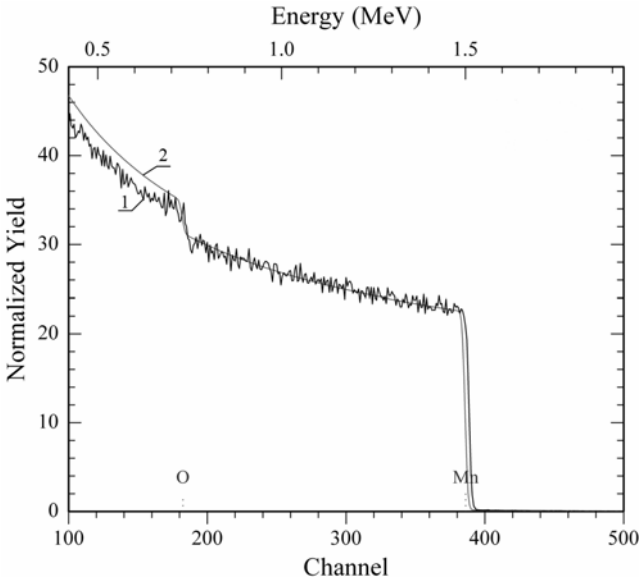

Figure 5.19: ***(1)*** *The RBS spectrum of an as-received MnO(100) single-crystal.* ***(2)*** *The fit to the spectrum made by using the RUMP program.*

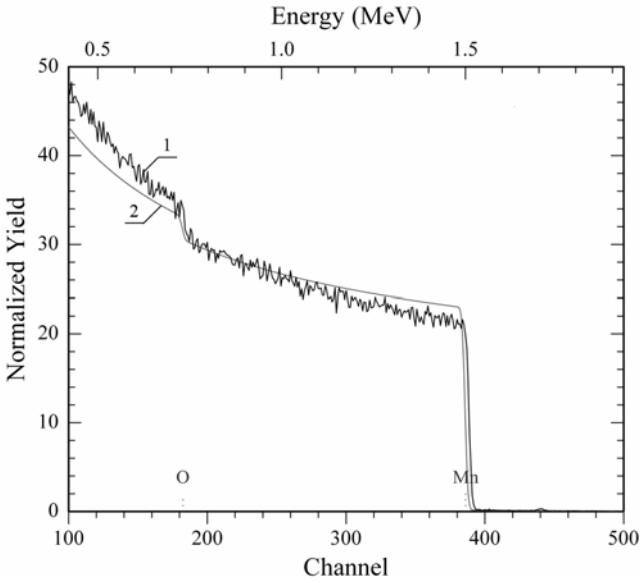

Figure 5.20: ***(1)*** *The RBS spectrum of an as-received MnO(100) single-crystal annealed at 700 °C for 85 min in O_2 (1 atm).* ***(2)*** *The fit to the spectrum made by using the RUMP program.*

5.4 Discussion

The annealing of the MnO(100) surface carried out in UHV and in the presence of oxygen resulted in several distinct surface structures. The genesis of the structures is yet not clearly understood and more detailed research is needed. Hence, at this point these questions are only qualitatively discussed.

Manganese element in its oxides, just as some other TM, due to its redox properties can easily alter its valence in response to changes in the environment. For instance, TM oxides can change the valence of the surface cations to compensate for the charge of missing oxygen atoms as a consequence of evacuation or mild chemical reduction, eventually resulting in a so-called *reduction-induced relaxation* [120]. Thus, it is very likely that during a temperature treatment under oxidizing or reducing conditions, several Mn oxides can be formed on the MnO(100) surface. They can coexist and/or progressively change into each other. As a result the morphology of the surface may exhibit a quite dynamic and complex behavior. Under thermodynamic equilibrium bulk oxide stoichiometries depend on the ambient oxygen partial pressure and temperature and can be calculated by phenomenological thermodynamics as, for example, was accomplished in [8] for Mn_xO_y system (Fig. 5.21). The stoichiometries and structure of oxide surfaces also depend on these parameters. However, the phase composition and the structure of oxide surfaces which can evolve and prevail under particular experimental conditions are difficult to predict only on the basis of thermodynamics. Moreover, if several Mn oxides may coexist on the surface they may interact with each other forming unique phases. In general, other factors can influence the formation of the phase composition of the surface, e.g., they can be driven by electrostatic forces and minimization of the number of dangling bonds [122, 123] or the formation of transients, kinetically stabilized phases is possible [124-126]. It should be noted that the surface structures on bulk single-crystals is far more difficult to stabilize than on thin oxide films [127 and ref. therein].

Before addressing the surface structures observed in the present study we believe that it is instructive to keep in mind the external shape (habit) of the macrocrystals of different Mn-oxides. The reason is that although the 2-D symmetry of the substrate surface is the most important factor determining the structure of the overlayer, the 3-D symmetry can also influence it, especially in case of oxide-on-oxide epitaxy. But here it is important to note that macroscopic crystals usually exhibit not the equilibrium shape but the growth shape. Their boundary planes (equal to the planes that belong to the equilibrium shape) result from slow growth in the normal direction, which is induced by the presence of a two-dimensional nucleation energy [128]. Instead microcrystals can reach their

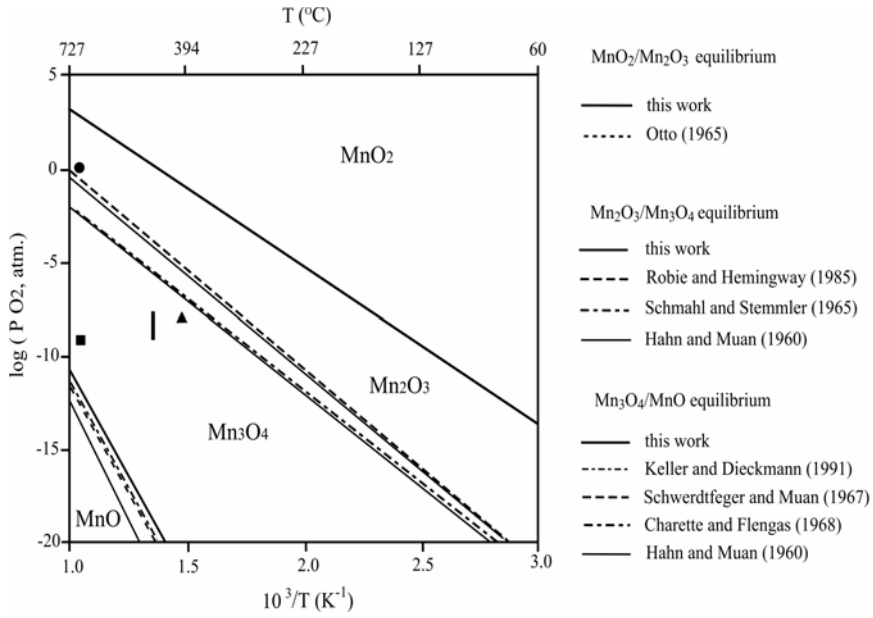

Figure 5.21: *Manganese-oxygen phase-stability diagram, p(O_2) given in atm. The different lines are the phase boundary proposed by different authors [8, and ref. therein]. The black square corresponds to the condition of the annealing carried out in oxygen p(O_2)= 3 × 10^{-6} mbar at 700 °C (see § 5.2.1, Fig. 5.9), the black triangle falls into the region of the experimental conditions 400°C and p(O_2)= 5×10^{-5} mbar (see § 5.2.2, Fig. 5.13), the black circle indicates the conditions of the experiments 700 °C and p(O_2)=1 atm (§ 5.2.3, Fig. 5.16), the black bar corresponds to the conditions of the experiments carried out in MnO(100)/Pd(100) system [120].*

equilibrium shape whose boundary planes are determined by their specific free energies. In addition the crystal habit may transform under the influence of different factors, for example, impurities which can influence the growth velocity. Thus, the growth shape of a macrocrystal can deviate from the equilibrium shape because the relative sizes of the various planes usually differ in the two shapes.

As can be seen in Fig. 5.1, all stable manganese oxides, except MnO_2 have a cubic and tetragonal symmetry. However, among naturally occurring manganese oxides only bixbyite - a manganese-iron oxide mineral $(Mn, Fe)_2O_3$ forms well-defined cubic crystals [21]. The Fe:Mn ratio is quite variable and many specimens have almost no iron. Another polymorphic modification – the mineral α-kurnakit (α-Mn_2O_3) having a face-centered tetragonal (*f.c.t.*) unit cell with lattice constants: $a=b$=8.85 Å, c=9.95 Å and c/a=1.124 occurs in nature as small rhombic crystals [129]. The transition temperature of α-Mn_2O_3 -> β-Mn_2O_3 (cubic, a=9.41 Å) is 670 °C [2]. Mn_3O_4 generally does not form well-defined single-crystals. Only rarely it occurs as superb, euhedral crystals, typically in the pseudo-octahedral habit of a

tetragonal bipyramid [130]. It was also found [131] that small particles of this oxide exhibit a cubic shape. Thus, from a geometric point of view on the microscale perhaps only MnO and Mn_2O_3 phases can be stabilized in cubic morphology. Another aspect concerning the morphology of micro/nano-structures arises when one phase can grow on top of another. Here the structure, and, hence, morphology of the overgrowing phase is determined by an epitaxial relationship between the phases. Epitaxial overgrowing takes place with pairs of crystals of whatever structure or bond type [128]. An especially interesting case is when the phases have a different crystal structure. An important example of relevance to the present study is the growth of Fe_3O_4 (tetragonal spinel) on a MgO(001) (rocksalt) substrate [132]. The STM study shows that instead of the difference in crystal structure between these two compounds, 200 nm-thick Fe_3O_4 films formed on polished MgO(001) at substrate temperature (250 °C) grow as pyramidal-shaped nanocrystalline islands, all with the same orientation and possessing a rather high density of steps. The sides if these islands are inclined by about 10° with respect to the substrate surface plane. Thus, one can speculate that if some of the above mentioned manganese oxide phases would nucleate and grow on the MnO(100) surface they all can exhibit a similar morphology (cubic symmetry). Consequently if several of them could coexist on the surface, it is apparently impossible to discriminate between them solely on a morphology basis.

The first peculiar surface structure that was found in our experiments is the RLS (see Fig. 5.4, Fig. 5.5 and Fig. 5.12). The structure is irreversible, since once formed at high temperatures, it persists upon cooling down to room temperature. As it is most distinctively developed following high temperature annealing (around 700 °C in UHV) and 1000 °C (1 atm Ar), its formation seems to be an activated process. On some locations of the surface the structure shows a remarkably regular morphology (see Fig. 5.7). Hence, it is reasonable to assume that it consists of many more simple regular structural units which can align in such a pattern. Such structural units may have as constituents MnO_6 octahedra in which cations are octahedrally coordinated by oxygen anions. In manganese oxides MnO_6 octahedra may be thought of as the fundamental building blocks united by either edge or corner sharing and assembling into a wide variety of ordered or disordered structures (chains, sheets or tree-dimensional units). The period of such a one dimensional chain is 0.28 nm [26]. Double and triple chains are formed when two or tree parallel chains are combined with each other by sharing edges of the MnO_6 octahedra. For instance, in MnO_2 the octahedra are connected by their sides. Also the octahedra in some manganese oxides can be distorted. For example, in β-MnO_2, a MnO_6 octahedron is slightly elongated with two long 1.894 (Å) and four short 1.882 (Å) Mn-O distances [133]. In hausmannite, the Mn^{3+} ion in octahedral position is subject to the Jahn-Teller

effect, resulting in the distortion of MnO_6 octahedra with four Mn-O distances of 1.930 (Å) and two of 2.290 (Å) [14, and ref. therein]. We suppose that the exact discrete dimensions of the RLS can be the manifestation of an ordering of a number of such octahedral units, and the way they are linked at their corners or edges specify the stoichiometry of the resulting structure. Apparently, it is topologically possible for such different structures to intergrow coherently, and the changes of stoichiometry can be accommodated by the intergrowth of the RLSs of different structure. We hypothesize that the RLSs also may be stabilized on the surface due to different kinds of defects present at the interface. Most of surface restructuring and reconstructions are attributed to the ordering of oxygen defects [134]. It is known that Mn-oxides become highly non-stoichiometric, when subjected to heating because of oxygen loss. The defect structure obviously may vary with oxygen deficiency which depends on temperature, gas pressure, impurities, etc. But which type of defect is dominant in a particular region of oxygen deficiency in MnO is not exactly known. It is known, however, that the cation defects are the majority defects in oxides having a rocksalt structure and the self-diffusion of metal ions is several orders of magnitude faster than that that of oxygen anions [135]. As predicted by lattice energy calculations the most stable defects in this type of oxides are complex defects arising from clustering of single defects. Depending on the conditions, the predominating defects can change, e.g., from Mn interstitials to vacancies and complex defects [135]. The results of the calculation of the energies of defect clusters in MnO using molecular orbital theory performed by Grimes *et al.* [136] indicate that relatively large extended defects of the zincblende type coordination are stable in MnO. The other kinds of defects represent dislocations. It is well known that dislocations can be arranged in networks with a cell structure of about 0.1 mm cell size [137]. They are sources and sinks of native defects. When a crystal is annealed, dislocations and defects interact with each other and eventually it can happen that dislocations and/or defects form some regular well aligned network inside the crystal. A high density of extended defects (dislocations) can significantly affect the mass and charge transport in solids. Possessing a high potential energy such a network of defects can act as a preferential nucleation site of a new oxide phase, different from the bulk periodicity. In addition, the surface of the annealed MnO(100) single-crystal due to cation or anion depletion in the near surface region can be unrelaxed. This may represent the driving force behind the formation and stabilization of a new, probably a polymorphic metastable surface phase (stoichiometric/non-stoichiometric), i.e. the RLS. The formation of RLS could lead to a more favorable surface structure which accommodates defects and lowers surface energy. In this context a perfect illustrative example of the possibility of the formation of different kinds of surface structures in manganese oxide system represents the

investigation by Netzer and coworkers [83], on the growth of Mn-oxide ultra thin films on a Pd(100) single-crystal surface. It was found that at an oxygen pressure of 2×10^{-7} mbar, epitaxially ordered bulk-type MnO films, terminated by (100) facets grew, whereas a pressure of 5×10^{-7} mbar and higher favored the formation of Mn_3O_4 crystallites. For a Mn-oxide coverage < 2 ML mainly two types of phases where found, which by using DFT calculations were assigned to interface-stabilized oxide layers with formal stoichiometries of Mn_4O_6 and Mn_4O_8. In the most recent report by this group [138] a complex phase diagram of Mn oxides on Pd(100) composed of nine different interface-stabilized phases was observed at Mn oxides coverages below 1 ML.

Another factor that can contribute to surface restructuring is surface contamination. It is known, that alkali and alkaline earth impurities segregating to the surface of some oxides can cause surface reconstructions [139]. In the present work, however, a detectable quantity of contaminants on the inspected surfaces has not been found except a small amount of carbon. It is widely accepted that densely packed oxide surfaces, such as MnO(100), are largely inactive. However, defects, particularly those associated with oxygen vacancies provide sites where adsorbates may bind strongly. It may be possible that a small concentration of carbon adsorbed on defects, for example, oxygen and/or manganese vacancies, can influence the balance of the MnO(100) surface energy during annealing in such a way that it rearranges with the formation of the surface structures possessing a lower total surface energy. It is important to note that (100) surfaces of rocksalt-structured oxides are known to be non-polar and it is generally accepted that they are not prone to reconstruct [139]. However, some non-polar oxide surfaces do reconstruct due to contaminations or a high temperature treatment [141-143]. For instance, by combined LEED and STM analysis [68], microfaceting of the CoO(100) surface upon annealing to 1100 K with the formation of (110) planes has been found. Considering the possibility of the MnO(100) surface to reconstruct, interesting results were reported by Langell and Cameron [59]. Since that work is of immediate relevance to the present study, its main results are presented here. The authors discovered that prolonged annealing of the surface causes the appearance of a (2×2) pattern. Because of the weak intensity of the LEED pattern, the (1×1) → (2×2) transition temperature could not be exactly determined. A (2×2) pattern appeared at an average temperature of 527 °C after 0.25-1 h annealing time and was stable down to 207 °C. Charging problems prevented the observation of a LEED pattern and thus conclusive statements about its stability could not be made. Further heating to 727 °C of the MnO(100)-(2×2) structure caused the reconstruction to a surface with a (6×6) unit cell. The LEED pattern of this structure was more intense than that corresponding to the (2×2) pattern. The (6×6) pattern persisted upon cooling to ambient temperature. Exposure of the

stoichiometric MnO(100) surface up to 900 L of CO, O_2 or NH_3 at temperatures in the range between 377-727 °C did not result in any detectable adsorption of the gases and no changes were observed in the XPS and AES spectra. Surface hydroxylation and adsorption of background contaminants were also excluded as a possible cause of the (2×2) and (6×6) reconstructions. Small amounts of calcium impurities were found to inhibit the (2×2) reconstruction but were disregarded as a reason for the surface reconstruction. It was concluded that the (2×2) and (6×6) structures are intrinsic properties of the stoichiometric MnO(100) surface and are not ordered defect or adsorbate overlayers. Hence, this investigation and our experiments indicate that the MnO(100) surface under certain conditions can exhibit a quite dynamic and complex behavior and the revealed phenomena deserve further study.

The next interesting surface structure which was registered in the present study is the TLPs (see Fig. 5.13 and Fig. 5.14). Unfortunately, the phase composition of the structure was not determined and only some preliminarily assumptions on this issue will be discussed in the following.

As can be judged from the Mn_xO_y bulk phase stability diagram, shown in Fig. 5.21, the conditions of the experiments where the TLPs were detected (400 °C and $p(O_2)=5\times10^{-5}$ mbar, Fig. 5.13) correspond to the region of stability of the Mn_3O_4 phase. According to Fritsch and Navrotsky [8], the enthalpy of oxidation at 298 K for the reaction $6MnO+O_2 \rightarrow 2Mn_3O_4$ is - 441.4 ± 5.8 (kJ/mol of oxygen) being the highest of the other possible reactions between oxygen and Mn-oxides. These data point out that the TLPs may be the manifestation of the Mn_3O_4 phase on the MnO(100) surface. As was found in the XRD experiments (see § 5.3.1), the as-received MnO(100) single-crystal probably contains a small amount of the Mn_3O_4 phase in the near-surface region. Taking this into account we speculate that the subcritical nuclei of these phase(s) at the surface or at some depth in the bulk can develop under certain conditions to faceted structures, i.e., the TLPs. In general, the presence of starting nuclei is not necessary and a new phase can also nucleate on any irregularity (defect) on the surface.

Rocksalt (MnO), spinel oxides (Mn_3O_4) and Mn_2O_3 are all closest packed in lattice oxygen and differ mainly in the filling of octahedral and tetrahedral sites with Mn^{2+}/Mn^{3+}. More specifically, Mn_3O_4 has tetragonally-distorted cubic lattice with a=8.149 Å and c=9.456 Å [144]. Actually, the crystal structure is $I4_1/amd$ with the a axes $1/2\sqrt{2}$ times 8.14 Å and the c axis remains the same, where the a axes of tetragonal spinel and $I4_1/amd$ are related by a rotation of 45° around the c - axis [145]. The oxygen sublattice in itself is thus *f.c.t.* with half the dimensions of the tetragonal spinel: 4.07 Å and 4.71 Å [146]. Since all of these oxides have cubic or tetragonal symmetry, it is possible that each of them can grow on another with cube-on-cube orientation under suitable conditions. For the transformation of

MnO to Mn_3O_4 it is necessary that a quarter of all Mn atoms shift less than the nearest neighbor Mn-O distance in MnO and a quarter have to diffuse out of the structure [147]. For the possibility of the formation of the Mn_3O_4 phase in annealed MnO samples prepared in the present study also point out the following data. As reported in [148 and ref. therein], Mn_3O_4 was systematically detected in $Mn_{1-z}O$ after quenching for non-stoichiometric compositions with $z > 0.002$. The manganosite samples in that study were prepared in CO_2/CO gas mixtures at temperatures between 1200 °C and 1450 °C, then quenched by either being dropped into water or cooled on the wall of a water jacket. The authors suggested that a simple point defect induces static shifts of the atoms and it causes some distortion of the O-M-O angles. This leads to the local reduction of the crystal's symmetry (cubic). The specific volumes of host lattice and defect clusters are very different. It is assumed that cooperative breaking of the bond angles O-M-O lead to dislocations and cracks on the surface of the grains of MnO that was also evidenced by the appearance of a dark color. Furthermore, in a multilayer sample obtained by oxidation of a Mn sheet, the precipitation of Mn_3O_4 has been registered in quenched non-stoichiometric samples. The crystalline shape depended on the non-stoichiometry. For nearly stoichiometric MnO, pillar or lamellar crystals were observed. If defects were present in large concentrations, the crystal showed an irregular polyhedral aspect. In several cases Mn_3O_4 has been observed in the grains of MnO. It was concluded that: (a) high temperature defects condition the morphology of the oxides; (b) Mn_3O_4 precipitates are quite independent (concerning the structure) of the host lattice in quenched samples. The authors also proposed a mechanism of the Mn_3O_4 phase formation: between the cold surface and the hot internal zone, the thermal stress gradient involves a continuous distortion. For large crystals a large stress gradient is involved, because of the large value of total distortion which is the sum of each cell distortions. The migration of metal ions and vacancies occurs in two opposite directions, according to so-called ascending diffusion. During quenching, some Mn^{2+} ions must jump from octa- to tetra positions, creating Mn_3O_4 islands. These jumps are easier if vacancies are present in large concentrations. The existence of the well-known (m/n) clusters (m vacancies, n interstitials) indicates that octa-tetra jumps are most likely in zones where vacancies are concentrated. Thus, around a Mn_3O_4 nucleus or cluster, these jumps can be collective and give rise to the Mn_3O_4 crystallite during quenching. It was speculated that the formation of superclusters or precipitates during the quenching process minimizes the angular distortion, and thus, the stress gradient from the center to the surface of the crystals. We believe that similar mechanisms of Mn_3O_4 formation as described above also could be realized in the annealed MnO(100) crystals examined in the present study.

Additional experimental evidence supporting the model that the TLP's may consist of the Mn_3O_4 phase is also provided by the most recent study by Bayer *et al.* [121], in which it was shown that Pd(100)-supported MnO(001) thin films with a typical thickness of 20 ML can be easily converted into Mn_3O_4(001) surfaces. Interestingly, the authors performed experiments under conditions (5×10^{-6}-2×10^{-5} mbar, T=770 K) very close to those applied in our study, as seen in the Mn_xO_y phase diagram (Fig. 5.21). It was revealed that the Mn_3O_4 phase develops in the form of elongated crystallites with the main axis oriented along the <110> symmetry directions. The conversion proceeds easily in both directions, such that annealing in UHV of Mn_3O_4(001) at 900-950 K leads to a pure and well-ordered MnO(001) film, which in turn can be readily reoxidized to the original Mn_3O_4(001). Another important result is that despite the rather large lattice mismatch of 9 %, MnO(001) is a favorable support for the formation of Mn_3O_4 (001)/MnO(001) interfaces due to the rather low strain energy (22 meV/atom) required for the expansion of the Mn_3O_4 planar lattice constant to the × 2 MnO value. DFT calculations suggest that the structural stability of the low index Mn_3O_4 surfaces follows the order: 001>110>100. Manganese terminated models were found significantly less stable than oxygen rich terminations for all orientations. Among two possible as-cleaved terminations of the (001) orientation of Mn_3O_4, a mixed oxygen and manganese surface with stoichiometry Mn_2O_4 was found to have the lowest surface energy and is 0.32-0.96 J/m^2 more stable than the other models considered. Different structural models for the Mn_3O_4(001)/MnO(001) interface have been tested. It was shown that a well-defined junction between MnO(001) and Mn_3O_4(001) is possible. The preferred model interface begins with a Mn_2O_4 terminated Mn_3O_4 layer accommodated onto the underlying MnO(001) substrate, with the Mn_3O_4 Mn atoms placed in atop site positions with respect to the MnO oxygen underneath.

We believe that the origin of the trapezoid-like structures may also be relevant to the understanding of the results reported by Hegeman *et al.* [149, and ref. therein]. The authors reported the formation of microprecipitates of MnO in a Cu matrix having octahedral shape due to termination of the precipitates by 8 MnO {111} facets. The formation of MnO before the appearance of Mn_3O_4 precipitates in Cu was explained by growth kinetics [147], although as stated, the latter oxide is thermodynamically more stable also as small coherent (dislocation free) and semi-coherent precipitates than MnO. The perimeter of one MnO faceted 3-D precipitate resting in a copper matrix was found to be formed by {111} planes. In this way the precipitate exhibits a trapezoid-like contour. The orientations of two of its facets were determined to be (857) and ($5\bar{1}7$) the presence of the latter one is, however, uncertain because it corresponds to a polar plane. In view of these data we are also tempted to suppose that although our

system differs substantially from the one described above, it is possible that under certain conditions similar precipitates of MnO phase can form on the MnO(100) surface. The TLPs in our study also are three-dimensional and are about 15-26 nm in height. Their formation and morphology can be also caused by the influence of growth kinetics. On the basis of thermodynamic considerations it was speculated [147] that if the formation of a precipitate within a certain volume is possible then MnO formation is preferred when the supply of oxygen is rate determining. But, after sufficient long oxidation times only the manganese concentration is limited and oxidation to higher oxidation states is more favorable. Interestingly, most of the precipitates registered in [147] were monophasic and exclusively single-crystalline. In most cases it was MnO, but a minor amount of Mn_3O_4 precipitates and some precipitates composed of both MnO and Mn_3O_4 phases were observed as well. The precipitates of the latter phase often consisted of several domains. Taking these data into account, we consider that the possibility for the TLPs to consist of a mixture of MnO and Mn_3O_4 phases cannot be ruled out.

By visual inspection of the AFM images it can be noted that the TLPs are quite ordered and interlocked with each other. Probably, the conditions of growth and stress phenomena (stress at the surface, volume stress or the interplay of these factors) induce collective process(es) which guide the orientation/ordering of these structures. Almost equal dimensions of the TLPs indicate that there is/are some mechanism(s) that limit(s) the growth of the islands. This may also point out that the TLPs are composed of some manganese oxide phase(s) which adopted equilibrium shape with a certain surface-volume ratio. To gain further insight into the shape of the TLP structures, more research should be performed.

The surface of the as-received MnO(100) sample (see § 5.2.3, Fig. 5.16) annealed at 700 °C and $p(O_2)$=1 atm for 85 min exhibited a network of irregularly shaped grains. As can be seen in Fig. 5.21, these experimental conditions are close to the border of the stability region of the Mn_2O_3 and Mn_3O_4 phases. At the same time XRD measurements [Fig. 5.17 (B)] revealed that this sample may contain the Mn_3O_4 phase. It should be noted that the Mn_3O_4 phase is isomorphic to the spinel-like γ-Mn_2O_3 phase (space group=$I4_1/amd$, a=8.150 Å, c=9.440 Å) [144] in which the oxide ions are in a cubic close-packed array. This phase is probably metastable [12, 14] and it represents a deficient arrangement of Mn_3O_4 with 8/3 cation vacancies per unit cell. It has a tetragonal symmetry with an axial ratio c/a=1.16 which is identical to Mn_3O_4 [150]. This makes it very difficult to distinguish between these phases due to very similar XRD patterns. Therefore, we suppose that the surface morphology observed by AFM may be related to these two phases.

If the TLPs represent the equilibrium shape of some of the Mn-oxides then it would be possible to construct their shape by using the Wulff construction, as described in § 3.4. However, to put it on a solid ground at present is not possible

because of the following reasons. The equilibrium shape of a TLP on a MnO(100) substrate is determined by the surface energies of the TLP's crystal facets (γ_{hkl}), the surface energy of the substrate (γ_s) and the interface energy between the TLP and the substrate (γ_i). Unfortunately, experimental values are lacking, although by some recent theoretical calculations the surface energies of some MnO surfaces have been established [151]. Furthermore, at present the phase composition of the these structures is unknown. Hence, only preliminarily assumptions regarding the construction of the TLP shape are presented.

In the paper of Ziółkowski [152] instead of the surface free energies, the surface enthalpies (J/m^2) of several low index surfaces of MnO in the so-called rigid lattice approximation were calculated to be: (001) - 2.56; (110) - 3.63; (120) - 3.44; (111) - 4.44; (112) - 4.19 and for β-MnO_2: (110) - 2.05; (100) and (010) - 2.9; (210) - 3.21; (101) - 3.08; (111) - 3.4; (001)-3.68. Note that low index surfaces have lower value of the surface enthalpy than high index surfaces. However, calculated in this way surface enthalpy does not take into account different relaxation phenomena that can occur at the near-surface region of a solid. Due to relaxation effects, the external shape of a nanoisland/nanocrystallite can deviate from the one based solely on the calculated surface enthalpies.

According to recently performed DFT calculations [151], the surface energies of the (100) and (110) surfaces of MnO are in the range of 0.71-0.86 J/m^2 for (100) and 1.31-1.73 J/m^2 for (110) surfaces, respectively. Thus, the calculated surface energy of the MnO surfaces with identical crystallographic orientation is a factor of about three lower compared with the surface enthalpies found by Ziółkowski. If we take into account the calculations performed in [151, 152] then free crystallites of the MnO phase in equilibrium should be cubes since the {100} planes have the lowest surface enthalpy and surface energy. Consequently, if we suppose that on the MnO(100) surface may form the precipitates of MnO phase, they should have a square shape. Deviation from the square morphology, i.e. trapezoid-like morphology may originate from different factors. For instance, deformation may be caused by different strain phenomena. In some cases the equilibrium shape of small crystallites is controlled by the competition between strain energy as a result of misfit at the interface and interfacial binding energies. Depending on the magnitude of the stress/strain, the elastic energy can become appreciable that results in deviations of the equilibrium shape associated with the Wulff construction. Then, the equilibrium shape can be predicted by approaches based on minimization of elastic strain energy [153, 154]. In addition, there also can be internal strains in small islands. Generally, surface stresses and volume stresses for particles > 10^{-5} cm are negligible [155]. Note that the TLPs just fall into the range of sizes where strain effects may influence the islands morphology. In this case it is possible to imagine the situation where by means of changing the

orientation of the low surface energy facets into higher surface energy facets the increase in strain may be balanced. In addition, as mentioned above, one cannot exclude the possibility that the TLPs are composed of a mixture of manganese oxides. Due to these and possibly other factors the crystallites may develop faces possessing higher surface energy on the external surface. Indeed, some of the TLPs are terminated by distinctly visible facets situated at their corners [marked with arrows, see, chapter 6: Fig. 6.8 (B)]. The TLPs are topped with distinct rectangular structures, which presumably represent an overgrowing manganese oxide phase. Also the amorphous-like perimeter of the TLPs is distinctly seen [Fig. 6.8 (B)].

It must be noted that when due to the condition of minimum crystallite energy the external shape of the equilibrated crystallite (e.g., TLP) should always be dominated by the face of the lowest surface energy, the other exposed face(s) do not necessarily appear in the order of increasing surface energy, i.e. some of them may be missing.

Finally, it is worth mentioning that many polymorphs of manganese oxides and oxyhydroxides are only 5-10 kJ/mol higher in enthalpy than the stable well-crystallized phases [156]. Recent studies [156, 157] show that the competition between surface enthalpy and the energetics of phase transformation can make micrometer-sized polymorphs metastable. In view of these data, one can envisage the possibility of the formation of a wide range of the polymorphic structures on the surfaces of manganese oxides.

5.5 Conclusions

The major findings of this chapter are as follows:

1. The first surface structure, termed the rippled-like consists of a regular pattern of elongated structures exhibiting at some surface locations a very regular periodicity and size (width). This structure appeared on the surface of an as-received MnO(100) single-crystal after annealing in UHV in the temperature range of 400-560 °C for several cycles of about 30 minutes (total annealing time 2.5 h), followed by annealing at 580 °C for 30 min. It appeared to be stable when the crystal was annealed in UHV for 1.5 h at 700 °C. However, after longer annealing under the same conditions it began to flatten out and broaden preserving its alignment on the surface. Subsequent annealing in the presence of oxygen $p(O_2)=3\times10^{-6}$ mbar at 700 °C for 4 h causes its disassembling to elongated smaller and flatter islands aligned similar to the initial structure. In addition to the rippled-like structure, occasionally symmetric square pits were observed on the surface. They ranged from 4 to 11 nm in depth with external sides of 20-50 nm,

with the majority having sides of 40 nm. The maximum dimension of the pits is *ca.* 50×50 nm. All the pits sides are inclined by about 45° to the pits' bottom plane as deduced from the line profiles of the AFM images. Annealing at higher temperature (650 °C) for 80 min caused the formation of a larger number of the pits.

2. Rapid thermal annealing of an as-received MnO(100) single-crystal in Ar (1 atm) at 1000 °C for 10 min causes a similar response of the surface as observed by annealing under UHV conditions, i.e. a similar rippled-like structure appears.

3. Rapid thermal annealing of an as-received MnO(100) sample at 1100 °C for 10 min in the presence of Ar (1 atm) causes the development of a grain-like structure on the surface with very broad smooth top regions. The height of the grain-like structure is ~ 40 nm. Subsequent annealing of the crystal for longer time (20, 40 min) under the same conditions causes the grain-like structure to widen preserving at the same time the smoothness of the top sides. Hut-like grains were observed at some locations of the crystal.

4. Annealing of an as-received MnO(100) single crystal in oxygen $p(O_2)=5\times10^{-5}$ mbar at 400 °C for 4 h leads to the formation of smooth-topped trapezoid-like pillars on the surface. A line profile made at the level of the median line of these structures indicated the width of 200-250 nm and the height of 20-25 nm. Sometimes intergrowth between the structures has been observed. Exposure to UHV conditions at room temperature for 4 days led to the appearance of roughness on the initially smooth-topped surfaces of the pillars. Taking into account the literature data and the Mn_xO_y bulk phase diagram, it is assumed that the trapezoid-like pillars may belong to the Mn_3O_4 phase or, alternatively, represent precipitate-like structures of the MnO phase. One also cannot rule out the possibility that the structures may consist of a mixture of MnO and Mn_3O_4 phases.

5. A MnO(100) single-crystal annealed in oxygen (1 atm) at 700 °C for 85 min exhibited a network of irregularly shaped large grains with a height of about 15 nm. This surface structure as determined from the XRD measurements and the Mn_xO_y bulk phase diagram may represent Mn_3O_4 and/or γ-Mn_2O_3 phase.

5.6 References

[1] A. F. Wells, *Structural Inorganic Chemistry,* 5th ed., (Oxford University Press, Oxford, UK, 1984).
[2] I. L. Knunyants, *Khimicheskaya entsyklopedia,* Vol. 2, (The Publishing House Sovietskaya entsyklopediya, Moskow, 1990) [in Russian].
[3] R. T. Downs, M. Hall-Wallace, Am. Mineral. **88**, 247-250 (2003).
[4] C. Picard, P. Gerdanian, J. Sol. State Chem. **11,** 190-202 (1974).
[5] A. Agopsowicz, J. L. Hitchcock, F. L. Tye, Thermochimica Acta **32,** 63-71 (1979).
[6] D. J. Morgan, A. E. Milodowski, S. St. J. Warne, S. B. Warrington, Thermochimica Acta **135,** 273-277 (1988).
[7] F. Tedjar, J. Guitton, Thermochimica Acta **181,** 13-22 (1991).
[8] S. Fritsch, A. Navrotsky, J. Am. Ceram. Soc. **79** (7), 1761-1768 (1996).
[9] C. Gonzalez, J. I. Gutiérrez, J. R. González-Velasco, A. Cid, A. Arranz, J. F. Arranz, J. Therm. Anal. **47**, 93-102 (1996).
[10] S. Fritsch, J. E. Post, A. Navrotsky, Geochim. Cosmochim. Acta **61**, 2613-2616 (1997).
[11] M. I. Zaki, M. A. Hasan, L. Pasupulety, K. Kumari, Thermochimica Acta **311,** 97-103 (1998).
[12] S. Fritsch, J. Sarrias, A. Rousset, G. U. Kulkarni, Mater. Res. Bull. **33** (8), 1185-1194 (1998).
[13] C. B. Azzoni, M. C. Mozzati, P. Galinetto, A. Paleari, V. Massarotti, D. Capsoni, M. Bini, Solid State Comm. **112,** 375-378 (1999).
[14] B. Gillot, M. El Guendouzi, M. Laarj, Mater. Chem. Phys. **70,** 54-60 (2001).
[15] Q. Zhao, W.-H. Shih, Microp. Mesop. Mat. **53,** 81-86 (2002).
[16] V. B. Fetisov, A. V. Fetisov, N. V. Korchemkina, L. A. Ovchinnikova, E. A. Pastukhov, and A. Ya. Fishman, Dokl. Phys. Chem. **387**, 291-293 (2002).
[17] K. M. Parida, S. B. Kanungo, Thermochimica Acta **66,** 275-287 (1983).
[18] Y. Chabre, J. Pannetier, Prog. Solid St. Chem. **23,** 1-130 (1997).
[19] J. E. Post, Natl. Acad. Sci. USA **96**, 3447-3454 (1999).
[20] T. E. Moore, M. Ellis, P. W. Selwood, J. Am. Chem. Soc. **72,** 856-866 (1950).
[21] Von H. Dachs, Z. Kristall. **107**, 370-395 (1956).
[22] L. S. Dent Glasser, I. B. Smith, Mineral. Magaz. **36**, 976-987 (1968).
[23] A. K. Lavrukhina, L. V. Yukina, *Analitischeskaya khimia margantsa,* (Moskow, Nauka, 1974) [in Russian].
[24] S. Turner, P. R. Buseck, Nature **304,** 143-146 (1983).
[25] J. H. Rask, P. R. Buseck, Am. Mineral. **71,** 805 (1986).
[26] N. Yamada, M. Ohmasa, S. Horiuchi, Acta Cryst. B **42**, 58-61 (1986).
[27] E. Chalmin, Ph. D. Thesis, Université de Marne-La-Vallée, France (2004).
[28] M. Angevaare, Ph. D. Thesis, Leiden University, The Netherlands (1991).
[29] R. Ramachandran, J. Mater. Sci., Mater. Electron. **13** (5), 257-262 (2002).

[30] Z. Gui, R. Fan, X.-H. Chen, Y.-C. Wu, Inorg. Chem. Comm. **4,** 294-296 (2001).
[31] T. Ahmad, K. V. Ramanujachary, S. E. Lofland and A. K. Ganguli, J. Mater. Chem. **14**, 3406-3410 (2004).
[32] J. Park, K. An, Y. Hwang, J.-G. Park, H.-J. Noh, J.-Y. Kim, Nat. Mater. **3**, 891-895 (2004).
[33] H. Yi-Fan, C. Fengxi, Z. Z. Yi, K. Ramesh, C. L. Wei, E. Widjaja, J. Phys. Chem. B **110** (48), 24450-24456 (2006).
[34] Z. Wu, K. Yu, Y. Huang, C. Pan, Y. Xie, Chemistry Central Journal **1**:8, 1-9 (2007). http://journal.chemistrycentral.com/content/1/1/8.
[35] Y. Chen, E. Johnson, X. Peng, J. Am. Chem. Soc. **129** (35), 10937-10947 (2007).
[36] M. Salavati-Niasaria, F. Davar, M. Mazaheric, Polyhedron **27** (17), 3467-3471 (2008).
[37] V. E. Henrich and P. A. Cox, *The surface science of metal oxides,* (Cambridge University Press, Cambridge, 1994).
[38] J. van Elp, R. H. Potze, H. Eskes, R. Berger, G. A. Sawatzky, Phys. Rev. B **44**, 1530-1537 (1991).
[39] M. Arai, T. Fujiwara, Phys. Rev. B **51** (3), 1477-1489 (1995).
[40] R. N. Iskenderov, I. A. Drabkin, T. L. Emel'yanova and Ya. Ksendzov, Fiz. Tverd. Tela **10**, 2573 (1968). [Sov.Phys.–Solid State **10**, 2031 (1969)].
[41] Ali Bakhshai, Ph.D. Thesis, The University of Texas at Arlington, USA (1982).
[42] A. Svane, O. Gunnarsson, Phys. Rev. Lett. **65**, 1148 - 1151 (1990).
[43] C. Franchini, V. Bayer, R. Podloucky, J. Paier, G. Kresse, Phys. Rev. B **72**, 045132 [6 pages] (2005).
[44] C. Franchini, R. Podloucky, J. Paier, M. Marsman, G. Kresse, Phys. Rev. B **75**, 195128 [11 pages] (2007).
[45] M. A. Langell, C. W. Hutchings, G. A. Carson, M. H. Nassir, J. Vac. Sci. Technol. A **14** (3), 1656-1661 (1996).
[46] T. Terakura, A. R. Williams, T. Oguchi, J. Kübler, Phys. Rev. B **52** (20), 1830-1833 (1984).
[47] J. Zaanen, G. A. Sawatzky, J. W. Allen, Phys. Rev. B **55** (4), 418-421 (1985).
[48] B. Hermsmeier, J. Osterwalder, D. J. Friedman, C. S. Fadley, Phys. Rev. Lett. **62** (4), 478-481 (1989).
[49] J. van Elp, J. L. Wieland, H. Eskers, P. Kuiper, G. A. Sawatzky, F. M. de Groot, T. S. Turner, Phys. Rev. B **44** (12), 6090-6103 (1991).
[50] L. Sangaletti, L.E. Depero, P. S. Bagus, F. Parmigiani, Chem. Phys. Lett. **245**, 463-468 (1995).
[51] P. S. Bagus, H. J. Freund, T. Minerva, G. Pacchioni, F. Parmigiani, Chem. Phys. Lett. **251**, 90-94 (1996).
[52] B. Fromme, M. Möller, C. Bethke, U. Brunokowski, E. Kisker, Phys. Rev. B **57** (19), 12069-12076 (1998).

[53] S. L. Dudarev, G. A. Botton, S. Y. Savrasov, C. J. Humphreys, A. P. Sutton, Phys. Rev. B **57** (3), 1505-1509 (1998).
[54] Ch. Henig, H. Merz, J. Elect. Spec. Rel. Phenom. **93**, 189-192 (1998).
[55] K. Dwight, N. Menyuk, Phys. Rev. B **119** (5) 1470-1479 (1960).
[56] L. Fiermans, R. Hoogewijs, J. Vennik, Surf. Sci. **47** (1), 1-40 (1975).
[57] R. C. Felton, M. Prutton, S. P. Tear, M. R. Welton-Cook, Surf. Sci. **88** (2-3), 474-478 (1979).
[58] K. Tsutsumi, H. Nakamori, K. Ichikawa, Phys. Rev. B **13** (2) 929-933 (1976).
[59] M. A. Langell and N. R. Cameron, Surf. Sci. **185** (1-2), 105-119 (1987).
[60] Ch. Henig, C. Untiet, H. Merz, J. Elect. Spec. Rel. Phenom. **76**, 547-551 (1995).
[61] T. Okazawa, Y. Kido, Surf. Sci. **556** (2-3), 101-108 (2004).
[62] S. M. Butorin, J.-H. Guo, M. Magnuson, P. Kuiper, J. Nordgren, Phys. Rev. B **54** (7), 4405-4408 (1996).
[63] R. J. Lad, V. E. Henrich, Phys. Rev. B **38** (15), 10660-10689 (1988).
[64] F. Buciuman, F. Patcas, R. Craciun, D. R. T. Zahn, Phys. Chem. Chem. Phys. **1**, 185-190 (1999).
[65] C. Mocuta, A. Barbier, G. Renaud, Appl. Surf. Sci. **162-163**, 56-61 (2000).
[66] S. L. Dudarev, L.- M. Peng, S. Y. Savrasov, J.- M. Zuo, Phys. Rev. B **61** (4), 2512-2506 (2000).
[67] H. A. E. Hagelin-Weaver, G. B. Hoflund, D. M. Minahan, G. N. Salaita, Appl. Surf. Sci. **235,** 420-448 (2004).
[68] S. Weichel, P. J. Møller, Surf. Sci. **399** (2-3), 219-224 (1998).
[69] M. R. Castell, S. L. Dudarev, C. Muggelberg, A. P. Sutton, G. A. D. Briggs, D. T. Goddard, Microscopy and Microanalysis **6**, 324-328 (2000).
[70] M. R. Castell, P. L. Wincott, N. G. Condon, C. Muggelberg, G. Thornton, S. L. Dudarev, A. P. Sutton, and G. A. D. Briggs, Phys. Rev. B **55** (12), 7859-7863 (1997).
[71] M. R. Castell, S. L. Dudarev, G. A. D. Briggs, A. P. Sutton, Phys. Rev. B **51** (11) 7342-7345 (1999).
[72] S. L. Dudarev, M. R. Castell, G. A. D. Briggs, A. P. Sutton, Physica B **229-261,** 717-718 (1999).
[73] H. Hosoi, K. Sueoka, K. Hayakawa, K. Mukasa, Appl. Surf. Sci. **157,** 218-221 (2000).
[74] H. Hosoi, M. Kimura, K. Hayakawa, K. Sueoka, K. Mukasa, Appl. Phys. A **72** (7), S23-S26 (2001).
[75] W. Allers, S. Langkat, R. Wiesendanger, Appl. Phys. A **72** (7), S27-S30 (2001).
[76] S. A. Chambers, Y. Liang, Surf. Sci. **420**, 123-133 (1999).
[77] H. Nishimura, T. Tashiro, T. Fujitani, J. Nakamura, Nippon Kagakkai Koen Yokoshu **78** (1), 392 (2000).
[78] H. Nishimura, T. Tashiro, T. Fujitani, J. Nakamura, J. Vac. Sci. Technol. A **18** (4), 1460-1463 (2000).

[79] G. A. Rizzi, R. Zanoni, S. Di Siro, L. Perriello, G. Granozzi, Surf. Sci. **462** (1-3), 187-194 (2000).
[80] F. Müller, R. de Masi, D. Reinicke, P. Steiner, S. Hüfner, K. Stöwe, Surf. Sci. **520** (3), 158-172 (2002).
[81] O. Nilsen, H. Fjellvåg, A. Kjekshus, Thin Sol. Films **444** (1-2), 44-51 (2003).
[82] Csiszár, Szilárd Istvan, Ph.D. Thesis, University of Groningen, The Netherlands (2005).
[83] G. Parteder, M. Leitner, F. Allegretti, B. Xu, M. Ramsey, S. Surnev, F. Netzer, V. Bayer, C. Franchini, R. Podloucky, Abstracts of oral presentations: *International Conference on Nanoscience and Technology*, p. 75 (Basel, 2006).
[84] M. F. Al-Kuhaili, J. Vac. Sci. Technol. A **24** (5), 1746-1750 (2006).
[85] S. Sachert, B. Bochmann, Ch. Hagendorf, S. Polzin, and W. Widdra, in *XII International Conference on Vibrations at Surfaces,* (Erice, Sicily, 2007).
[86] F. Allegretti, C. Franchini, V. Bayer, M. Leitner, G. Parteder, B. Xu, A. Fleming, M. G. Ramsey, R. Podloucky, S. Surnev, and F. P. Netzer, Phys. Rev. B **75**, 224120 (2007).
[87] M. Nagel, I. Biswas, P. Nagel, E. Pellegrin, S. Schuppler, H. Peisert, T. Chassé, Phys. Rev. B **75**, 195426/1-6 (2007).
[88] M. Nagel, L. Zhang, H. Peisert and T. Chassé, Microchim. Acta **156,** 27-31 (2007).
[89] M. Nagel, I. Biswas, H. Peisert, T. Chassé, Surf. Sci. **601** (18), 4484-4487 (2007).
[90] A. Chassé, Ch. Langheinrich, F. Müller, S. Hüfner, Surf. Sci. **602** (2), 597-606 (2008).
[91] Ch. Hagendorf, S. Sachert, B. Bochmann, K. Kostov, W. Widdra, Phys. Rev. B **77**, 075406 [8 pages] (2008).
[92] U. Hartmann, *An Elementary Introduction to Atomic Force Microscopy and Related Methods*, (University of Saarbrücken, Germany, 1997).
[93] F. J. Gießibl, Habilitationsschrift, University of Augsburg, Germany (2000).
[94] R. García, R. Pérez, Surf. Sci. Rep. **47**, 197-301 (2002).
[95] E. C. Voogt, Ph. D. Thesis, Department of Chemical Physics and Nuclear Solid State Physics, University of Groningen, The Netherlands (1998).
[96] M. Iwamoto, Y. Yoda, N. Yamazoe, T. Seiyama, J. Phys. Chem. **82** (24), 2564-2569 (1978).
[97] C. B. Azzoni, M. C. Mozzati, P. Galinetto, A. Paleari, V. Massarotti, D. Capsoni, M. Bini, Solid State Commun. **112** (7), 375-378 (1999).
[98] W. Levason, C. A. McAuliffe, Coord. Chem. Rev. **7**, 353-384 (1972).
[99] H. Yi-Fan, K. Ramesh, L. Chen, E. Widjaja, S. Chilukoti, C. Fengxi, J. Phys. Chem. C **111** (7), 2830-2833 (2007).
[100] H. Yi-Fan, C. Luwei, K. Ramesh, E. Widjaja, S. Chilukoti, I. K. Surjami, J. Chen, J. Catal. **253** (2), 261-268 (2008).
[101] http://www.csrri.iit.edu/periodic-table.html
[102] http://xdb.lbl.gov/

[103] JCPDS card no. 24-734, (Hausmannite, Mn_3O_4), JCPDS card no. 7-230 (MnO), JCPDS card no. 18-803 (γ-Mn_2O_3).
[104] M. S. Seehra and G. Srinivasan, J. Appl. Phys. **53** (11), 8345-8347 (1982).
[105] T. J. Chuang, C. R. Brundle, D. W. Rice, Surf. Sci. **59**, 413-429 (1976).
[106] G. A. Sawatzky, D. Post, Phys. Rev. B **20**, 546-1555 (1979).
[107] R. P. Gupta, S. K. Sen, Phys. Rev. B **10**, 71-79 (1974).
[108] S. P. Kowaltczyk, L. Ley, F. R. McFeely, D. A. Shirley, Phys. Rev. B **11**, 1721-1727 (1975).
[109] M. Oku, K. Hirokawa, J. Elect. Spec. Rel. Phenom. **7,** 465-473 (1975).
[110] V. Young, L. Z. Zhao, Chem. Phys. Lett. **102** (5), 455-458 (1983).
[111] B. R. Strohmeier, D M. Hercules, J. Phys. Chem. **88**, 4922-4929 (1984).
[112] V. Di Castro, G. Polzonetti, Chem. Phys. Lett. **139** (2), 215-218 (1987).
[113] V. Di Castro, G. Polzonetti, J. Elect. Spec. Rel. Phenom. **48,** 117-123 (1989).
[114] V. Di Castro, S. Ciampi, Surf. Sci. **331-333** (1), 294-299 (1995).
[115] C. Sharfschwerdt, J. Kutscher, F. Shneider, M. Neumann, S. Tougaard, J. Elect. Spec. Rel. Phenom. **60,** 321-335 (1992).
[116] T. Kendelewicz, C. S. Doyle, X. Carrier, G. E. Jr. Brown, Surf. Rev. Lett. **6** (6), 1255-1263 (1999).
[117] C. D. Wagner, A. Joshi, J. Elect. Spec. Rel. Phenom. **47,** 283-313 (1988).
[118] A. A. Audi, P. M. A. Sherwood, Surf. Interf. Anal. **33** (3), 274-282 (2002).
[119] W. E. Wallace, Q. Zhong, J. Genzer, R. J. Composto, D. A. Bonnell, J. Mater. Res. **8** (7), 1629-1634 (1993).
[120] D. T. J. Hurle, *Handbook of crystal growth,* Vol. 1, *Thermodynamics and kinetics,* (Elsevier, Amsterdam, 1993).
[121] V. Bayer, R. Podloucky, C. Franchini, F. Allegretti, B. Xu, G. Parteder, M. G. Ramsey, S. Surnev, F. P. Netzer, Phys. Rev. **76**, 165428 (2007).
[122] A. Barbieri, W. Weiss, M. A. Van Hove, G. A. Somorjai, Surf. Sci. **302** (3), 259-279 (1994).
[123] W. Weiss, A. Barbieri, M. A. Van Hove, G. A. Somorjai, Phys. Rev. Lett. **71**, 1848-1851 (1993).
[124] J. Gustafson, A. Mikkelsen, M. Borg, E. Lundgren, L. Köhler, G. Kresse, M. Schmid, P. Varga, J. Yuhara, X. Torrelles, C. Quirós, and J. N. Andersen, Phys. Rev. Lett. **92**, 126102 (2004).
[125] E. Lundgren, J. Gustafson, A. Mikkelsen, J. N. Andersen, A. Stierle, H. Dosch, M. Todorova, J. Rogal, K. Reuter, M. Scheffler, Phys. Rev. Lett. **92**, 046101 (2004).
[126] U. Diebold, Mat. Res. Soc. Symp. Proc. **654**, AA51.1-AA51.9 (2001).
[127] H.-J. Freund, H. Kuhlenbeck, V. Staemmler, Rep. Prog. Phys. **59**, 283-347 (1996).
[128] G. A. Wolff, J. G. Gualtieri, Am. Mineral. **47**, 562-584 (1962).
[129] *Bolshaya sovetskaya entsyclopediya* Vol. **26***,* B. A. Vvedenskiy (ed.), 258 (Moskow, 1954).

[130] V. Baron, J. Gutzmer, H. Rundlöf, R. Tellgren, Am. Mineral. **83**, 786-793 (1998).
[131] A. Maltha, Ph. D. Thesis, Leiden University, The Netherlands (1994).
[132] S. A. Chambers, S. A. Joyce, Surf. Sci. **420**, 111-122 (1999).
[133] T. Kohler, T. Armbruster, E. Libowitzky, J. Sol. State Chem. **133**, 486-500 (1997).
[134] H. H. Kung, *Transition metal oxides: Surface Chemistry and Catalysis,* Vol. 45, (Elsevier, Amsterdam, 1989).
[135] P. Kofstad, Oxidation of metals **19** (3/4), 129-149 (1983).
[136] R. W. Grimes, A. B. Anderson, A. H. Heuer, J. Am. Ceram. Soc. **69** (8), 619-623 (1986).
[137] D. Hull and D. J. Bacon, *Introduction to dislocations,* 3rd ed., Vol. 37, (Pergamon Press, Oxford, 1984).
[138] F. Li, G. Parteder, F. Allegretti, C. Franchini, R. Podloucky, S. Surnev, F. P. Netzer, J. Phys.: Condens. Matter **21** 134008 [11pages] (2009).
[139] K.-I. Fukui, Y. Iwasawa, Surf. Sci**. 441** (2-3), 529-541 (1999).
[140] C. Noguera, *Physics and Chemistry of Oxide Surfaces*, (Cambridge University Press, 1996).
[141] V. E. Henrich, Surf. Sci. **57** (2), 385-392 (1976).
[142] H. Nörenberg, F. Dinelli, G. A. D. Briggs, Surf. Sci. **446**, L83-L88 (2000).
[143] L. E. Firment, Surf. Sci. **116** (2), 205-216 (1982).
[144] F. A. Al Sagheer, M. A. Hasan, L. Pasupulety, M. I. Zaki, J. Mater. Sci. Lett. **18**, 209-211 (1999).
[145] B. J. Kooi, J. Th. M. De Hosson, Acta mater. **48**, 3687-3699 (2000).
[146] B. J. Kooi, H. B. Groen, J. Th. M. De Hosson, Acta Mater. **46** (1), 111-126 (1998).
[147] B. J. Kooi, J. Th. M. De Hosson, Acta mater. **46** (6), 1909-1922 (1998).
[148] J.-R. Gavarri, J. Arabski, S. Jasienska, J. Janowski, C. Carel, J. Sol. State Chem. **58**, 56-70 (1984).
[149] J. B. J. W. Hegeman, B. J. Kooi, H. B. Groen, J. Th. M. De Hossom, J. Appl. Phys. **86** (7), 3661-3669 (1999).
[150] J. B. Goodenough and A. L. Loeb, Phys. Rev. **98** (2) 391-408 (1955).
[151] V. Bayer, C. Franchini, R. Podloucky, Phys. Rev. B **75**, 035404 (2007).
[152] J. Ziółkowski, Surf. Sci. **209** (3), 536-561 (1989).
[153] M. Kato, T. Fuji, Acta Metall. Mater. **42** (9), 2929-2936 (1994).
[154] J. K. Lee, JOM **49** (12), 37-40 (1997).
[155] N. Cabrera, Surf. Sci. **2**, 320-345 (1964).
[156] A. Navrotsky, Geochem. Trans. **4** (6), 34-37 (2003).
[157] A. Navrotsky, L. Mazeina, J. Majzlan, Science **319** (5870), 1635-1638 (2007).